Understanding Arctic Ocean circulation: a review of ocean dynamics in a changing climate

Mary-Louise Timmermans[1] **and John Marshall**[2]

[1]Department of Geology and Geophysics, Yale University, New Haven, Connecticut, USA
[2]Department of Earth, Atmospheric and Planetary Sciences, Massachusetts Institute of Technology, Cambridge, Massachusetts, USA

Key Points:

- Major features of Arctic Ocean circulation are reviewed and interpreted theoretically
- Fundamental ocean dynamics are set in the context of a changing Arctic climate
- We describe how Arctic dynamics might change in the future

Corresponding author: Mary-Louise Timmermans, `mary-louise.timmermans@yale.edu`

Abstract

The Arctic Ocean is a focal point of climate change, with ocean warming, freshening, sea-ice decline and circulation that link to the changing atmospheric and terrestrial environment. Major features of the Arctic and the interconnected nature of its wind- and buoyancy-driven circulation are reviewed here by presenting a synthesis of observational data interpreted from the perspective of geophysical fluid dynamics (GFD). The general circulation is seen to be the superposition of Atlantic Water flowing into and around the Arctic basin, and the two main wind-driven circulation features of the interior stratified Arctic Ocean: the Transpolar Drift Stream and the Beaufort Gyre. The specific drivers of these systems and their associated GFD are explored. The essential understanding guides an assessment of how Arctic Ocean structure and dynamics might fundamentally change as the Arctic warms, sea-ice cover declines and the ice that remains becomes more mobile.

1 Introduction

The Arctic Ocean, centered over the north pole and surrounded by land, is covered entirely by a thin (order 1 m) layer of sea ice in winter, which can shrink by up to 2/3 every summer. Arctic summer sea-ice appears to be in rapid decline in recent decades (D. Perovich et al., 2019). Moreover the north polar regions are warming faster than the global-mean (Overland et al., 2019) — a phenomenon known as Arctic amplification — further accelerating Arctic change. For these reasons the Arctic is particularly vulnerable to climate change. In the coming decades we may expect to enter a new regime, in which the interior Arctic Ocean is entirely ice free in summer and sea ice is thinner and more mobile in winter (e.g., T. W. Haine & Martin, 2017). Some climate model scenarios suggest the Arctic Ocean may be seasonally ice free by ∼2050 (Collins et al., 2013). A seasonally ice-free Arctic will have vast implications for Arctic oceanography, the marine ecosystems it supports and the larger-scale climate. It will also have wide-ranging consequences for Arctic communities, geopolitics and policy as Arctic coastal environments and sea routes change and Arctic resources become more accessible. Urgent challenges will be to implement effective observing strategies, and synthesize observations in theoretical and modeling analyses to better understand the ocean's role and interrelationships in the Arctic system.

In this review we summarize some major aspects of Arctic Ocean physical oceanography by presenting key observations in a common format, discuss the cause of its general circulation and how it might change as the Arctic enters a new sea-ice regime. The physical oceanography is complex and, due to the presence of sea ice, difficult to observe. The first ocean measurements from the central Arctic Ocean were made during Fridtjof Nansen's 1893-1896 drift of the Fram (Nansen, 1897). Observations revealed it to be a vast deep basin, and confirmed the existence of the Transpolar Drift Stream, the flow of ice and water from the coast of Siberia across the Arctic to the North Atlantic via the east coast of Greenland. It was during Nansen's expedition that the observation was made that sea ice drifts somewhat to the right of the prevailing wind direction — an observation that was the foundation of Ekman's theory describing the friction-Coriolis force balance in geophysical fluid boundary layers (Ekman et al., 1905). Rudels et al. (2012) provides a concise review of the exploration history leading to the general picture in the mid-1900s of the Arctic being a deep ocean characterized by complex bathymetry and relatively warm water of Atlantic Ocean origins underlying relatively cool and fresh surface waters capped with ice (Figure 1).

The Arctic Ocean receives inflows from the Atlantic and Pacific oceans and North American and Siberian rivers. Its stratification is set by salinity (there is a halocline rather than a thermocline) with melting and freezing of sea ice being a central player in the freshwater cycle and in the mediation of the wind stress acting at the surface. Familiar, textbook paradigms of ocean circulation, such as *Sverdrup balance*, that underpin theories of the mid-latitude oceans, are not applicable in the Arctic where the north-south gradient of the Coriolis parameter is vanishingly small. The rapid changes that are presently underway have raised new questions about the Arctic Ocean's future dynamics, the relative importance of influences exterior and interior to the Arctic, and the complex ocean-ice-atmosphere interactions and feedbacks which involve and evolve as sea-ice declines. Our review is led by observations, and we apply the underlying theory of geophysical fluid dynamics to shed light on contemporary circulation characteristics presenting what we consider to be the key ideas. We then speculate how the fundamental dynamics may be transformed under continued Arctic change.

Our review is outlined as follows. In Section 2 we describe the geographical and bathymetric setting of the Arctic, how it connects to the rest of the world ocean, Arctic Ocean surface properties, and the wind patterns driving the circulation. Two key centers of meteorological action are the Beaufort High and the Icelandic Low, introducing anticyclonic and cyclonic vorticity tendencies, respectively. In Section 3 we desribe the Arctic Ocean temperature and salinity structure and buoyancy forcing (dominated by surface freshwater fluxes). Mixing and stirring in the Arctic Ocean are described in Section 4. The observed circulation of warm, salty Atlantic Water entering and circulating around the Arctic basin is described in Section 5. Its transformation within the semi-enclosed Arctic basin is associated with mixing of cold, fresh water from above (Section 5.1). The wind provides a source of energy for mixing, but also its cyclonic curl external to the basin (associated with the Icelandic Low) plays an important role in drawing Atlantic Water, strongly steered by topography, in to the Arctic basin (Section 5.2). Interior to the Arctic basin, the two main wind-driven circulation features are the Transpolar Drift Stream and the anticyclonic Beaufort Gyre, under the influence of the Beaufort High, as discussed in Sections 6 and 7, respectively. In Section 8 we describe how the Arctic system is changing as the Earth warms and how those changes may manifest themselves in the circulation dynamics. In Section 9, we attempt to synthesize the overall ocean structure and dynamics in a conceptual framework within which we can contemplate and reconcile ongoing and future Arctic change.

2 Geographical setting and Arctic Ocean surface properties

The Arctic Ocean, along with the Greenland, Iceland and Norwegian seas (the Nordic Seas) are together referred to as the *Arctic Mediterranean* because, as shown in Figure 1a, it is a large deep basin of water surrounded by land and shallower channels (see e.g., Sverdrup, Johnson, Fleming, et al., 1942). The main entry to the Arctic Mediterranean is marked by the Greenland-Scotland Ridge. Relatively warm and salty Atlantic Ocean water flows across the Greenland-Scotland Ridge into the Nordic Seas (Hansen et al., 2008). Atlantic water enters the Arctic via Fram Strait and the Barents Sea Opening (see e.g., Beszczynska-Möller, Fahrbach, Schauer, & Hansen, 2012; Ingvaldsen, Loeng, & Asplin, 2002; Schauer, Fahrbach, Osterhus, & Rohardt, 2004). The only oceanic gateway between the Pacific and Arctic oceans is Bering Strait where Pacific Water inflows provide an important source of fresh water and heat to the Arctic Ocean (T. W. N. Haine et al., 2015; Woodgate, Weingartner, & Lindsay, 2010). Waters leave the Arctic Ocean via straits in the Canadian Arctic Archipelago (e.g., LeBlond, 1980; Münchow, Melling,

& Falkner, 2006), and in the East Greenland current that flows south on the west side of Fram Strait (e.g., Woodgate, Fahrbach, & Rohardt, 1999).

The bathymetric and topographic complexity within the Arctic is extreme and exerts strong controls on circulation pathways, ventilation and exchange processes between Arctic basins. Bathymetry also influences the spatial variability of diapycnal mixing and baroclinic instability, as described in Section 4. The roughly 4000 m deep Arctic basin is divided by the Lomonosov Ridge, with a mean depth of around 1500 m (Cochran, Edwards, & Coakley, 2006), separating the Eurasian and Canadian basins. These two basins are subdivided into the Amundsen and Nansen basins (separated by the Gakkel Ridge) and the Makarov and Canada basins (separated by the $\sim$2200-m-deep Alpha and Mendeleyev Ridges), Figure 1.

The Arctic is under the influence of two major wind-patterns: the Beaufort High centered over the Canadian Basin, introducing anticyclonic tendencies, and the Icelandic Low centered just outside of the Arctic basin inducing cyclonic tendencies and orchestrating the Arctic gateway to the Atlantic (Figure 2c). Wind-stress curl patterns are such that there is broad Ekman downwelling over much of the Arctic Ocean, and relatively strong upwelling over the Nordic Seas, indicated by the blue and red colors in Figure 2c, respectively. Sea-ice motion (Figure 2a, white arrows), and surface ocean geostrophic flow (Figure 2d), generally follow the wind with the anticyclonic flow of the Beaufort Gyre (the dominant upper-ocean circulation feature of the Canadian Basin) and Transpolar Drift Stream being clearly evident.

Arctic sea-ice cover extends throughout the Arctic Ocean in winter (approximately where white arrows are present in Figure 2a), and is characterized by an average thickness of around 2 m. Sea-ice has a large seasonal cycle, with summer sea-ice extent in recent years generally around one-third of the winter extent. The winter maximum extent occurs in March, while the sea-ice minimum is in September. The August 2018 sea-ice distribution is shown in Figure 2b (colored white) together with the August mean extent for 1981-2010 (black contour). Since 1979 (the start of the satellite record) a linear trend indicates summer (September) sea ice has been declining at a rate of about 1 million square kilometers per decade, with sea ice covering about 4.5 million square kilometers in September in recent years (e.g., D. Perovich et al., 2019; D. K. Perovich & Richter-Menge, 2009; Richter-Menge, Jeffries, & Osborne, 2018). Declining sea-ice volume (i.e., a shift to a thinner, more mobile sea-ice pack) accompanies these sea-ice area losses. In the 1980s, average winter (fall) sea-ice thickness was around 3.6 m (2.7 m), while in 2018, average winter (fall) ice thickness was $\sim$2 m (1.5 m) (Kwok, 2018). The loss of Arctic sea ice is not only a conspicuous indicator of climate change, it also sustains a fundamental global climate feedback through its influence on Earth's planetary albedo (Pistone, Eisenman, & Ramanathan, 2014). Arctic Ocean warming (e.g., I. V. Polyakov et al., 2010; Timmermans, 2015; Timmermans, Toole, & Krishfield, 2018; Woodgate, 2018), freshening (e.g., A. Proshutinsky et al., 2009; Rabe et al., 2014), and changing stratification, circulation dynamics, and momentum transfer to the ocean (e.g., Meneghello, Marshall, Timmermans, & Scott, 2018; Peralta-Ferriz & Woodgate, 2015; I. V. Polyakov et al., 2017) all link to the sea ice.

The amount and mobility of sea ice is of great relevance to the balance of forces that drive the large-scale ocean circulation, because it acts as a critical mediator of wind-stress in the Arctic, as explored in Section 7. Further, sea-ice cover, sea-surface salinity and temperature are also strongly coupled. Surface salinities are much fresher in the Arctic Ocean compared to the north Pacific and Atlantic oceans (Figure 2a), the broad result of northward transport of atmospheric fresh water from equatorial regions, with contributions from seasonal sea-ice melt and relatively fresh ocean flows from the Pacific Ocean. Arctic Ocean sea-surface temperatures are at the freezing point (around -2°C for seawater) in winter and in regions where sea-ice persists year round. Outside of the winter months, an opening in the sea-ice pack can leave the ocean exposed to direct solar forcing, increasing sea-surface temperatures. These warmed surface waters can melt the surrounding sea ice, exposing more open water and a positive feedback (the *ice-albedo feeback*) ensues. Summer sea-surface temperatures at the ice-free margins of the Arctic basin can be up to a few degrees above 0°C, with higher sea-surface temperatures (again several degrees above 0°C) in the vicinity of Pacific and Atlantic Water inflows (Figure 2b and see Timmermans and Ladd (2019)). Owing to the halocline stratification, which we describe next, the warm waters originating in the Pacific and Atlantic oceans do not need to be confined to the surface Arctic Ocean, and can reside at depth.

3 Arctic Ocean stratification and buoyancy forcing

A trans-Arctic section crossing from the Pacific to the Atlantic oceans illustrates the essential Arctic Ocean water-mass distribution and stratification: relatively cold, fresh water overlies relatively warm, salty water (Figure 1b). Marked gradients in temperature, salinity and density are confined to the top few hundred meters of the water column which features various components of the Arctic halocline (Figure 3). We consider the potential density surface $\sigma = 27.4$ kg m^{-3} to approximately represent the base of the halocline, and plot its depth across the Arctic Ocean (Figure 3a). In the Canada Basin, this isopycnal surface is as deep as $\sim$200 m, marking the imprint of the anticyclonic Beaufort Gyre which is in thermal wind balance with lateral density gradients. Also evident is the signature of the Transpolar Drift Stream at the confluence of the Canadian and Eurasian Basins.

Representative vertical profiles of temperature, salinity and density in the Canadian and Eurasian Basins illustrate the details of the upper water column (Figure 3b). Underlying the surface mixed layer ($\lesssim$ 50 m deep), is a relatively warm near-surface layer in the Canadian Basin, absent in the Eurasian Basin. It derives from the $\sim$1 Sv (1 Sv= 10^6 m^3 s^{-1}) northward flow through the $\sim$50 m deep and $\sim$80 km wide Bering Strait (e.g., Woodgate et al., 2010). This layer, which has temperatures in the range -1 to 1°C, and sits at around 50 to 100-m depth in the Canadian Basin (Figure 3b,c), is called Pacific Summer Water since it ventilates the region in summer (e.g., Steele et al., 2004; Timmermans et al., 2014). Below the Pacific Summer Water layer in the Canadian Basin sits relatively cooler and saltier Pacific Winter Water (e.g., Pickart, Weingartner, Pratt, Zimmermann, & Torres, 2005), which ventilates the region in winter (Figure 3b,c). The base of the Pacific Winter Water layer is approximately bounded by the $\sigma = 27.4$ kg m^{-3} surface. In both the Canadian and Eurasian basins, a layer of warm Atlantic-origin water, characterized by temperatures around 0 - 3°C (colored red in Figure 3c), resides between roughly 150 and 500-m depth, at or below the $\sigma = 27.4$ kg m^{-3} surface. We discuss these Atlantic-origin waters in detail in Section 5.

A defining feature of the Arctic Ocean with a profound influence on the behavior of the Arctic system and climate is that it is predominantly salinity-stratified. This basic stratification of fresher waters overlying saltier waters, separated by a strong halocline, is known as a β-ocean, where β refers to the saline contraction coefficient. By contrast, the subtropical α-oceans (where α refers to the thermal expansion coefficient) have their stratification set mainly by temperature, with warmer waters overlying cooler waters. This broad stratification distinction, evident at around 45^0N in both the Pacific and Atlantic sectors (Figure 1b), is a vital aspect of ocean and climate relevance; for example, sea ice can only grow at the surface of β-oceans where the salinity stratification inhibits deep convection — an α-ocean would convect (see E. C. Carmack, 2007). In the mid-latitude α-oceans, there is a net warming and evaporation. The atmospheric moisture is transported polewards where it precipitates over the high-latitude β-oceans. The non-linear equation of state of seawater also factors in this distinction with α increasing with temperature, such that it is about an order of magnitude larger at 20°C compared to its value at much colder (near freezing) Arctic Ocean temperatures (see Timmermans & Jayne, 2016). In Section 8 we return to discuss this $\alpha - \beta$ transition in the context of a changing Arctic Ocean under increasingly Atlantic influence.

River discharge, predominantly from the six main Arctic rivers (the Ob, Yenisey, Lena, Kolyma, Yukon, and Mackenzie rivers), is a major source of fresh water to the Arctic Ocean (Holmes et al., 2012; McClelland, Holmes, Dunton, & Macdonald, 2012). While the Arctic Ocean constitutes only 1% of the World's ocean by volume, it catches around 10% of its river discharge (Aagaard & Carmack, 1989). The Arctic Ocean also receives fresh water through net precipitation (e.g., Serreze et al., 2006) and relatively fresh water from the Pacific Ocean via Bering Strait (Woodgate & Aagaard, 2005). In the annual mean, the partitioning of this freshwater input is around 1/2 river discharge, 1/4 Pacific water inflow and 1/4 net precipitation (E. C. Carmack, 2000; E. C. Carmack et al., 2016; T. W. N. Haine et al., 2015; Serreze et al., 2006); much smaller contributions (less than a few percent) derive from meltwater fluxes from Greenland and northward sea-ice fluxes through Bering Strait (T. W. N. Haine et al., 2015). Surface fresh water from all of these sources is drawn toward the center of the Canadian basin by the anticyclonic winds of the Beaufort High, ensuring the maintenance of the Arctic's strong halocline stratification (Figure 3).

As Arctic sea ice grows and moves, and brine is rejected, there is a distillation of fresh water. While some fraction of this fresh water returns to liquid form during sea-ice melt each summer, export of sea ice from the Arctic Ocean is a sink of fresh water (in solid form) (see Aagaard & Carmack, 1989). Fresh water leaves the Arctic via ocean and sea-ice flows through channels in the Canadian Arctic Archipelago and through Fram Strait. Around 1/3 of the total freshwater export is in liquid form via each of Fram Strait and Davis Strait, with 1/4 of the total exported in solid sea-ice fluxes through Fram Strait (T. W. N. Haine et al., 2015).

The Arctic Ocean warms in summer via surface-water heating in ice-free regions that is dominated by solar radiation (e.g., D. K. Perovich, Richter-Menge, Jones, & Light, 2008). The net surface heat flux is the sum of incoming shortwave radiation, longwave emission, and sensible plus latent heat fluxes. Throughout the year, vertical sensible and latent heat fluxes are small contributions (having magnitudes $\lesssim 10$ W m^{-2}) (e.g., Serreze et al., 2007). The net longwave flux is larger (around 50 W m^{-2} upward) and remains approximately constant throughout the year. The net shortwave component has a strong seasonal cycle, dominating in summer when average values over the Arctic Ocean are around 150 W m^{-2} downward. Incoming solar radiation is effectively zero between October and March (e.g., Serreze et al., 2007).

The Arctic Ocean also receives heat via warm inflows from the Atlantic and Pacific oceans (e.g., Beszczynska-Möller et al., 2012; Woodgate, Weingartner, & Lindsay, 2012). At the low temperatures of Arctic waters, α is sufficiently small that ocean temperature does not strongly influence ocean dynamics. This may change as the ocean continues to warm, and we discuss potential implications of this in Section 8. While ocean temperature may have only a weak influence on ocean dynamics, it is crucially important to the fate of Arctic sea-ice cover should heat be mixed to the surface. We therefore now outline the primary mixing processes at work in the Arctic.

4 Mixing and stirring in the Arctic Ocean

The Arctic Ocean exhibits a variety of ocean mixing processes that differ from the mid-latitudes because of the presence of sea ice, the high latitude, and the distinct halocline stratification structure with warm water underlying cooler water. These processes include convection by surface buoyancy fluxes resulting from brine rejection during ice formation, turbulence driven by stress at the ice-ocean interface, mixing by internal waves (where the internal wave field is affected by the high latitude Coriolis effect and sea-ice cover), and double-diffusive mixing (see the review of these processes by Padman, 1995). The Arctic Ocean is also baroclinically unstable and the mean flow emerges only after averaging over an energetic mesoscale and submesoscale.

4.1 Small-scale diapycnal processes

Arctic Ocean mixing levels are critical to the fate of sea ice because the ocean heat stored at depth is enough to melt the entirety of the Arctic sea ice (G. A. Maykut & Untersteiner, 1971). However, this would require some mechanism (e.g., dissipation of internal wave energy or double diffusion or vertical eddy heat flux) to mix that heat to the surface layer in contact with sea ice. At present, the Arctic Ocean exhibits generally low mixing rates compared to the mid-latitude ice-free oceans (e.g., D'Asaro & Morison, 1992; Rainville & Winsor, 2008).

There is relatively weak tidal forcing in the Arctic and most of the region is above the critical latitude north of which the semi-diurnal tide can propagate freely. Topographic waves generated over bathymetric slopes and rough topography, forced by the tides (Kowalik & Proshutinsky, 1993), are the main source of energy for higher tidal dissipation observed over topography (Holloway & Proshutinsky, 2007; Kowalik & Proshutinsky, 1995; Luneva, Aksenov, Harle, & Holt, 2015; Padman, Plueddemann, Muench, & Pinkel, 1992; Rippeth et al., 2017). Sea-ice cover is present for most of the year and acts as a buffer to wind-driven momentum input to the upper ocean; further, internal wave energy can be dissipated under sea ice (Morison, Long, & Levine, 1985; Pinkel, 2005). In the fully-ice covered winter months, inertial wave energy and shear are generally weaker than in the seasonal absence of sea ice (Dosser, Rainville, & Toole, 2014; Halle & Pinkel, 2003; Rainville & Woodgate, 2009). In the summer months, even though winds are weaker than in winter, median inertial wave amplitudes are perhaps 10 to 20% larger than in winter. The additional energy is a consequence of increased atmosphere to ocean momentum transfer in open water regions and the absence of sea-ice damping of internal waves (e.g. Dosser & Rainville, 2016). In Section 8, we discuss the implications of Arctic sea-ice loss on ocean mixing levels.

Microstructure measurements indicate turbulent kinetic energy dissipation ϵ in the halocline of the deep basins to be around $5{\times}10^{-10}$ to $2{\times}10^{-9}$ W kg^{-1} (Fer, 2009; Lenn et al., 2009; Lincoln et al., 2016; Rippeth et al., 2015). These values may be compared to typical midlatitude ocean thermocline values of around 10^{-9} W kg^{-1} (J. M. Toole, Schmitt, & Polzin, 1994). In the Arctic's continental shelf regions, ϵ is estimated to be two orders of magnitude larger than over the abyssal plain; in the region just north of Svalbard, for example, $\epsilon \sim 3 - 20 \times 10^{-8}$ W kg^{-1} (Rippeth et al., 2015). This can be compared to values estimated by Ledwell et al. (2000) of around 10^{-8} W kg^{-1} over the rough topography of the Mid-Atlantic Ridge. Elevated rates of dissipation of kinetic energy are also found over the Canada Basin shelf regions where $\epsilon \approx 2 \times 10^{-8}$ W kg^{-1} (Lincoln et al., 2016; Rippeth et al., 2015).

Diapycnal diffusivity K_ρ takes values around 10^{-4} m^{2}s^{-1} at the base of the mixed layer to $\sim 1{-}7{\times}10^{-6}$ m^2 s^{-1} in the strongly-stratified halocline away from topographic features (D'Asaro & Morison, 1992; Fer, 2009; Padman & Dillon, 1989; Rainville & Winsor, 2008). In model studies, the Atlantic Water circulation direction and strength is found to be highly sensitive to the level of vertical mixing. Zhang and Steele (2007) find values of $K_\rho \approx 10^{-6}$ m^2 s^{-1} yield Atlantic Water circulation patterns and water properties that best agree with climatology (values typically appropriate for midlatitudes, around 10^{-5} m^2 s^{-1}, returned an anticyclonic Atlantic Water circulation, inconsistent with observations).

Low mixing levels in the interior basin allow for the persistence of a double-diffusive staircase at the top boundary of the Atlantic Water layer (see Figure 3b, inset panel), and double-diffusive fluxes are the main mechanism for vertical heat transport from the Atlantic Water. Vertical heat fluxes across the double-diffusive staircases in the central basins are only in the range 0.02$-$0.3 W m^{-2}, however (Guthrie, Fer, & Morison, 2015; Padman & Dillon, 1987, 1989; Shibley, Timmermans, Carpenter, & Toole, 2017; Sirevaag & Fer, 2012; Timmermans, Toole, Krishfield, & Winsor, 2008). For context, these heat fluxes are about one tenth of the mean surface ocean heat flux to the sea ice. Annual average ocean-to-ice heat fluxes are around $3 - 5$ W m^{-2}, with monthly-average values up to 30 W m^{-2} in July and August, with maximum values up to 60 W m^{-2} (R. A. Krishfield & Perovich, 2005; G. Maykut & McPhee, 1995; Wettlaufer, 1991). In these regions, summer solar heating of the surface ocean layer (in ice-free regions or through thin ice) provides the main heat source for ocean-to-ice heat fluxes (Fer, 2009; G. Maykut & McPhee, 1995; G. A. Maykut & Untersteiner, 1971; Timmermans, 2015; J. M. Toole et al., 2010).

A well-defined double-diffusive staircase is absent around most Arctic Ocean continental shelf-slope regions (i.e., coinciding with pathways of the Atlantic Water) (Shibley et al., 2017), likely because of higher mixing levels in those regions (e.g., Rippeth et al., 2015). Staircases do appear at the eastern boundary of the Eurasian Basin and in the vicinity of the east Siberian continental slope, where double-diffusive heat fluxes are estimated to be higher (order 1 W m^{-2}) compared to interior basin values (Lenn et al., 2009; I. V. Polyakov et al., 2012). Note that ocean-to-ice heat fluxes can be order 100 W m^{-2} where the Atlantic Water enters the Arctic Ocean and where stratification and turbulence levels are not amenable to the formation of a double-diffusive staircase (Peterson, Fer, McPhee, & Randelhoff, 2017).

Related to the double-diffusive staircase at the top boundary of the Atlantic Water layer, are prominent thermohaline intrusions underlying the staircase and emanating from the core of the Atlantic Water (e.g., Bebieva & Timmermans, 2017; E. Carmack et al., 1998; Rudels, Kuzmina, Schauer, Stipa, & Zhurbas, 2009). These intrusions have a lateral component of motion, driven partly by double-diffusive vertical buoyancy flux divergences, and carry warm Atlantic Water from the boundaries to the interior basins (Bebieva & Timmermans, 2019; F. McLaughlin et al., 2004; Walsh & Carmack, 2003; Woodgate, Aagaard, Swift, Smethie Jr, & Falkner, 2007). Walsh and Carmack (2003) estimated lateral diffusivities associated with these thermohaline instrusions to be around 50 m^2 s^{-1}. In this way, diapycnal mixing can redistribute Atlantic Water heat laterally, with Atlantic Water intrusions taking around a decade to propagate across the Canada Basin (see for example Bebieva & Timmermans, 2019).

While diapycnal mixing of deeper ocean heat can delay the onset of freezing at the start of the ice-growth season, and yield reductions in total sea-ice thickness (e.g., G. A. Maykut & Untersteiner, 1971; D. K. Perovich et al., 2011; Steele, Ermold, & Zhang, 2008; Timmermans, 2015), its role in the large-scale ocean circulation is less clear. Diapycnal mixing has been presumed to play a role in driving the Atlantic Water inflow to the Arctic Ocean, as we will discuss in Section 5.1. Lateral eddy fluxes, on the other hand, have been shown to be a key player in the fundamental dynamics of the Beaufort Gyre, as we discuss in Section 7.

4.2 Eddies, baroclinic instability and isopycnal eddy diffusivity

Baroclinic eddies are a ubiquitous feature of the Arctic Ocean, which is observed to have a vigorous mesoscale and submesoscale eddy field (e.g., Carpenter & Timmermans, 2012; Kozlov, Artamonova, Manucharyan, & Kubryakov, 2019; Manley & Hunkins, 1985; G. E. Manucharyan, Thompson, & Spall, 2017; Mensa, Timmermans, Kozlov, Williams, & Özgökmen, 2018; Pnyushkov, Polyakov, Padman, & Nguyen, 2018; Spall, Pickart, Fratantoni, & Plueddemann, 2008; Timmermans, Toole, Proshutinsky, Krishfield, & Plueddemann, 2008; M. Zhao et al., 2014). Water column kinetic energy in the Arctic's halocline is dominated by eddies (B. Zhao & Timmermans, 2018), and we expect eddy buoyancy fluxes and along-isopycnal stirring by eddies to play an important role in the general circulation, as will be shown in Section 7.

The horizontal length scale that tends to characterize eddies and baroclinic instabilities of the ocean mean state is the first baroclinic Rossby radius of deformation, $R_d = ND/f$ where D is the vertical scale over which horizontal currents vary, f is the Coriolis parameter, and $N^2(z) = -(g/\rho_0)(\partial\rho/\partial z)$ is the stratification. Chelton, Deszoeke, Schlax, El Naggar, and Siwertz (1998) estimated R_d from hydrographic climatology by solving the quasi-geostrophic equations for a given stratification profile, $N^2(z)$. In Figure 4a we follow the methodology of Chelton et al. (1998) to compute R_d from Arctic Ocean climatology (see also Nurser and Bacon (2014); M. Zhao et al. (2014)). Shallow shelf regions are generally characterized by a much smaller deformation radius (of order a few kilometers) than the deep basins (where it is around 7 - 15 km), while variations in R_d between deep basins arise due to stratification differences (see M. Zhao et al., 2014). The Beaufort Gyre is more strongly stratified than the Eurasian Basin water column; typical values of R_d in the Beaufort Gyre region are around 15 km, twice as large as values in the deep Eurasian Basin. Observed eddies have horizontal scales which are roughly consistent with values of R_d. Eddies in the Canadian Basin have larger diameters than those in the Eurasian Basin (M. Zhao et al., 2014). We note that the horizontal scales of the energy-containing eddies may differ from the deformation radius because there is an inverse energy cascade. The upscale energy transfer on a β-plane may be arrested at the Rhines scale, which can characterize a transition to a Rossby wave regime (see Rhines (1975) and the discussion by Tulloch, Marshall, Hill, and Smith (2011)). In the Arctic Ocean, the Coriolis parameter f is approximately constant (i.e., an f-plane), and the Rhines scale is set by topographic beta. Nevertheless, the scales apparent in Figure 4a highlight the challenges for numerical modeling of ocean processes in the region where model grid scales must be smaller than a few kilometers to resolve mesoscale eddies.

Related to the Rossby deformation radius, we may analyze hydrography to examine the linear stability characteristics of the mean state of the Arctic Ocean. If the mean current has speed U, then we expect an inverse timescale (growth rate) $\omega \sim U/R_d$. This may be expressed in terms of the Richardson Number, $Ri = N^2D^2/U^2$, where D is the vertical scale over which U varies, as $\omega \sim f/\sqrt{Ri}$ (the Eady growth rate). More detailed calculations calibrated against linear stability yield (see Smith, 2007; Tulloch et al., 2011):

$$\omega = f\sqrt{\frac{1}{H}\int_H^0 \frac{dz}{Ri(z)}}, \tag{1}$$

where the Richardson number $Ri(z)$ may be estimated as a function of the stratification and the thermal wind shear, $Ri = N^2/\left[(\partial u/\partial z)^2 + (\partial v/\partial z)^2\right]$. Smith (2007) examines hydrographic climatology for the global oceans south of 60^0N and shows (1) to be a good approximation of the linear growthrates of the fastest growing modes in the thermocline.

If the generation of eddies is associated with baroclinic instability, we expect the Eady timescale ω^{-1} to be short where there is anomalously high eddy kinetic energy and/or weak stratification. Around the Arctic basin margins, timescales are of the order of a few days or shorter, while in the central Canada Basin/Beaufort Gyre and Nordic Seas regions, Eady timescales computed from (1) are 8-10 days (Figure 4b). This is consistent with satellite-derived eddy kinetic energy estimates, which show the shelf and boundary-current regions to have higher eddy kinetic energy compared to the interior Canada Basin and Nordic Seas (Armitage et al., 2017). Notably, the central Eurasian Basin exhibits shorter timescales (faster growth rates) than the Canada Basin, and this may be attributed to the significantly weaker stratification there (Figure 3b); satellite-derived estimates of eddy kinetic energy are not available for the Eurasian Basin.

For the Beaufort Gyre, satellite-based estimates of eddy kinetic energy, and the application of mixing-length theory, have been used to infer eddy diffusivities (Armitage et al., 2017). A similar approach has been used to estimate eddy diffusivities in the Beaufort Gyre from eddy kinetic energy based on in-situ mooring velocity measurements (Meneghello, Marshall, Cole, & Timmermans, 2017). These studies yield eddy diffusivity values in the range 100-600 m^2 s^{-1}, decaying from higher to lower values with depth (Meneghello et al., 2017). As described in Section 7, eddy diffusivities of such magnitude suggest that eddy-induced circulation can be as large as the Eulerian circulation, with important implications for the general circulation and tracer transport in the Arctic.

Water-mass distribution, stratification structure and strength, mixing and lateral eddy processes, are intimately connected with ocean circulation pathways, which we describe next, beginning with an analysis of the circulation of Atlantic Water into and around the Arctic basin.

5 The Circulation of Atlantic Water in the Arctic

On route to the Arctic Ocean, Atlantic waters cross the Scotland-Greenland Ridge and propagate into the Nordic Seas in branches stemming from the North Atlantic Current extension of the Gulf Stream. In the Norwegian Sea, the northward flow follows two topographically steered western and eastern branches of the Norwegian Atlantic Current (e.g., Orvik & Niiler, 2002). These waters enter the Arctic Ocean at the $\sim$2600 m deep, $\sim$450 km wide, Fram Strait, which is the deepest connection between the Nordic Seas and the Arctic Ocean (Figure 5). At Fram Strait there is an exchange flow between inflowing Atlantic Water and outflowing relatively cooler and fresher upper Arctic Ocean waters (Figure 5c). The West Spitsbergen Current (WSC) carries relatively warm and salty Atlantic Water north (around 7 Sv) into the Arctic Ocean on the eastern side of Fram Strait, with a recirculation within Fram Strait (see e.g., Beszczynska-Möller et al., 2012; Schauer et al., 2004). The East Greenland Current (EGC) flows south (around 9 Sv) out of the Arctic Ocean along the western side of Fram Strait (de Steur, Hansen, Mauritzen, Beszczynska-Möller, & Fahrbach, 2014). Net transport through Fram Strait has been estimated to be several Sv to the south, with month-to-month variability that can be as large (Schauer & Beszczynska-Möller, 2009). Atlantic Water also enters the Arctic Ocean from the Nordic Seas via the Barents Sea Opening ($\sim$ 2 Sv) (Ingvaldsen et al., 2002; Schauer, Loeng, Rudels, Ozhigin, & Dieck, 2002).

Where Atlantic Water enters the Arctic Ocean through Fram Strait and the Barents Sea Opening, the overlying sea ice melts and the upper-most waters undergo a cooling and freshening transformation such that the Atlantic Water temperature maximum resides at depth within the Arctic Ocean (e.g., Rudels, Anderson, & Jones, 1996; Untersteiner, 1988). The spatial distribution of maximum Atlantic Water temperature has been used to infer its cyclonic pathway around the boundary of the Eurasian Basin (e.g., L. Coachman & Barnes, 1963) and is shown in Figure 5a,b,d. There is believed to be a recirculation within the Eurasian Basin, as schematized by Rudels, Jones, Anderson, and Kattner (1994), see their Figure 9. Atlantic Water penetrates the Makarov and Canada basins (where the Atlantic Water core referenced by the depth of the temperature maximum is located around 400 m depth, Figure 5d) and circulates cyclonically around the basin margins, clearly guided by bottom topography. Mooring measurements indicate Atlantic Water boundary current speeds to be around 2 to 4 cm s^{-1} (Woodgate et al., 2001). This is consistent with transient tracer data which suggest Atlantic Water propagation from the Eurasian Basin to the southern Canada Basin (a distance of around 6000 km) takes around 7.5 years (Mauldin et al., 2010).

Below the Atlantic Water layer, the Arctic Ocean's deep and bottom waters are generally inferred (from sparse measurements) to follow a cyclonic pathway in both the Eurasian and Canadian basins, in the same sense as the intermediate Atlantic Water (e.g. Aagaard, 1981; Rudels, 2015). Deepest waters also exhibit variable bottom-trapped currents and waves (Aagaard, 1981; Timmermans, Rainville, Thomas, & Proshutinsky, 2010; B. Zhao & Timmermans, 2018). Note that, distinct from the Atlantic Water boundary current, there also exist narrow, energetic, seasonally-varying boundary currents, with typical speeds around 15 cm s^{-1}, trapped at the shelf breaks in the Eurasian and Canadian basins (e.g., Aksenov et al., 2011; Dmitrenko et al., 2016; Nikolopoulos et al., 2009; Pickart, 2004); the properties of these shelf-break currents depend strongly on local and remote winds and buoyancy forcing.

Ascertaining what drives the Atlantic Water inflow and its circulation within the Arctic Ocean has been the subject of study since Nansen (1902) first identified warm subsurface water within the Arctic Ocean as having originated in the North Atlantic. We now briefly review two bodies of work that explore the mechanisms from rather different perspectives: the first, using an estuary framework, invokes wind-driven mixing interior to the Arctic to draw water in; the second invokes winds exterior to the Arctic to drive water in to the Arctic following bathymetric contours.

5.1 An estuary framework

The earliest models of Arctic Ocean circulation were *estuarine-like* (see e.g., Aagaard, Swift, & Carmack, 1985), motivated by the idea that the Arctic is a semi-enclosed basin in which the inflow from the Nordic Seas is balanced by an outflow of relatively fresh water, and this exchange flux depends upon the level of mixing within the Arctic basin (Figure 6). The circulation is driven by buoyancy; winds only play a role in mixing upper and intermediate waters in the estuary basin.

Stigebrandt (1981) modeled the upper Arctic Ocean water column as a function of buoyancy input, wind-driven mixing and topographic control at the connecting straits (here, primarily Fram Strait and Lancaster Sound) that are sufficiently wide that the effects of Earth's rotation are important. His model couples conservation of volume and salt, and a weir formula for the hydraulically-controlled (and rotationally-influenced) volume flow through the straits, plus a horizontally uniform vertical entrainment velocity that is a function of both wind-driven mixing and convection. This estuarine description of the circulation shows how the buoyancy input and mixing in the interior Arctic Ocean can uphold a steady exchange flow between the Arctic Ocean and Nordic Seas.

Consider an idealized system in which there is a volume flux Q_1 of Polar Water (upper layer of salinity S_1) leaving the Arctic Ocean (e.g., via Fram Strait) and a volume flux Q_2 of Atlantic Water (lower layer, of salinity S_2) entering the Arctic Ocean from the Nordic Seas (Figure 6). For a flux through the Bering Strait of Q_B (of salinity S_B) and net freshwater flux Q_f (approximately the sum of river influxes and net precipitation, minus a sea-ice export flux from the Arctic Ocean) into the upper layer in the Arctic Ocean, conservation of volume may be written

$$Q_1 = Q_2 + Q_B + Q_f. \tag{2}$$

For a hydraulically controlled flow of the upper layer (of thickness H_1) through Fram Strait, the flow rate is given by (Whitehead, 1998)

$$Q_1 = \frac{g' H_1^2}{2f}, \tag{3}$$

where $g' = g(\rho_2 - \rho_1)/\rho_0$ is the reduced gravity between the Polar Water ρ_1 and Atlantic Water ρ_2 layers (ρ_0 is a reference density). A good approximation is given by $g' = g\beta(S_2 - S_1)$, which neglects temperature influences on density. Equation (3) applies because Fram Strait (around 500 km wide) is much wider than the internal Rossby deformation radius, with typical parameter values yielding $(2g'H_1)^{1/2}/f \approx 10$ km, in accord with Figure 4a. Conservation of salt in the upper layer is given by

$$Q_1 S_1 = Q_2 S_2 + Q_B S_B. \tag{4}$$

The remaining model component is an entrainment flux of lower layer water across the halocline (Figure 6) which may be written in terms of the area A of the halocline and an entrainment velocity w_e as:

$$Q_2 = w_e A. \tag{5}$$

Specification of w_e requires some quantification of the mixing processes. Mixing between the Atlantic Water and the Polar Water may be driven by processes ranging from double-diffusive convection to shear-driven mixing by winds and sea-ice motion, to surface buoyancy fluxes driving convection, such as sea-ice growth generating dense brine. Stigebrandt (1981) formulates the following expression for entrainment velocity

$$w_e = \frac{2.5 u_*^3}{g\beta(S_2 - S_1)H_1} + \gamma \frac{Q_f S_1}{A(S_2 - S_1)}. \tag{6}$$

The first term on the right relates the injection of kinetic energy to the interface to a change of potential energy of the system (mixing), where u_* is a friction velocity characterizing the mixing levels. The second term quantifies the contribution (scaled by a parameter γ) to w_e by surface freswater buoyancy fluxes.

Choosing typical values of external parameters ($A = 10^{13}$ m^2, $Q_B = 1.5{\times}10^6$ m^3 s^{-1}, $S_B = 32.4$, $\gamma = 0.05$ and $S_2 = 35$; see Stigebrandt (1981)), the system (2) to (6) may be solved to determine the Atlantic Water influx Q_2, and the properties of the upper layer H_1 and S_1 exiting the Arctic Ocean through Fram Strait as functions of net freshwater input Q_f and mixing levels (quantified by specifying u_*), Figure 6b. For larger net freshwater fluxes Q_f into the Arctic Ocean (i.e., river influxes and net precipitation dominate over a sea-ice export flux), the outflowing upper layer is thinner and fresher, and there is a smaller Atlantic Water volume influx Q_2 to the Arctic Ocean. Further, for fixed Q_f, an increase in mixing gives rise to a thicker, saltier upper layer exiting the Arctic Ocean, and a larger volume influx of Atlantic Water. For a range of appropriate parameters, the solutions generally yield plausible results for the exchange flow at Fram Strait. Rudels (1989) employs the formalism of Stigebrandt (1981) and incorporates spatially-variable mixing (water-mass transformations in the shelf regions) to deduce a magnitude for the Atlantic Water inflow to the Arctic Ocean and strength of the stratification that depends on the buoyancy input.

These general ideas have been extended further by considering the Arctic Mediterranean to be a double-estuary (Eldevik & Nilsen, 2013; Lambert, Eldevik, & Haugan, 2016). This conceptualizes cooling and dense water formation in the Nordic Seas as a negative estuary, and positive buoyancy forcing (freshwater input) in the Arctic Ocean (i.e., a positive estuary). Heat loss in the Nordic Seas drives an overturning circulation there (Mauritzen, 1996) while the freshwater input to the north drives an estuarine circulation with the Atlantic Water layer. Lambert et al. (2016) find that because of the

Arctic estuary circulation, an Atlantic Water inflow to the Arctic can persist even in the absence of deep convection in the Nordic Seas. This is an important point in the context of discussions related to Atlantic Water heat entering the Arctic being influenced by the strength of the Atlantic Meridional Overturning Circulation (AMOC). Based on climate model simulations, it has been put forward, for example, that a strengthened AMOC has been partly responsible for Arctic Ocean warming and sea-ice loss (e.g., Delworth et al., 2016).

The estuary view of Arctic circulation has been invoked in an attempt to explain the presence of the halocline. Indeed, it is in accord with the traditional model of the Arctic halocline (Aagaard et al., 1985): the required mixing within the Arctic basin is associated with the entrainment of ambient water by plumes that flow down continental slopes powered by concentrations of dense brine formed by ice formation over the continental shelves, as represented by the upward circular arrows in Figure 6a. The structure of the interior Arctic halocline, however, requires additional processes, such as advection by wind-driven circulation and lateral eddy fluxes, to bring the ventilating dense water away from continental slopes and into the interior. Spall (2013) presents a conceptual model in which the halocline structure and Atlantic Water flow are set by the combined effects of horizontal eddy fluxes taking water from the basin boundaries to the interior and vertical diapycnal mixing in the interior basin. In his idealized simulations, an effectively barotropic Atlantic Water inflow (and cyclonic Atlantic Water boundary current) is balanced by outflowing cooler water including a surface-intensified fresh outflow. The essential common feature between this and other models of the Arctic Mediterranean estuary is that buoyancy forcing and mixing in the interior drives the Arctic-Nordic Seas exchange.

Bathymetric influences (aside from those of the straits) and recirculations within the Arctic basin are not represented in estuary models. Nor do they account for recirculations in the vicinity of the connecting straits. Further, it is unclear whether the required mixing between the surface fresh layers and the inflowing Atlantic Water is realistic. In an alternative framework, the wind directly drives the topography-following Atlantic Water circulation. In the next section, we describe studies which have shown how the prevailing wind field over the Arctic Mediterranean is such that the wind-stress curl can set the observed ocean transport.

5.2 Wind-driven flow along f/H contours

Wind-stress curl patterns over the Arctic are such that there is broad Ekman downwelling over much of the interior basin, with relatively strong upwelling over the Nordic Seas (Figures 2c and Figure 7a). Over most of the tropical and subtropical oceans, wind-stress curl is balanced by the depth-integrated meridional transport, i.e., Sverdrup balance (e.g., Gray & Riser, 2014; Wunsch, 2011). However, where topography has a strong influence, and in the higher latitudes where the β-effect (here, β refers to the meridional gradient of the Coriolis parameter) is negligible, Sverdrup balance does not hold. Nøst and Isachsen (2003) analyzed Arctic Mediterranean wind forcing and hydrographic climatology to show that patterns of Ekman downwelling and upwelling differ markedly from the depth-integrated meridional transport predicted based on Sverdrup balance. Instead of being constrained by the β-effect, the potential vorticity-conserving barotropic flow is controlled by sea-floor topography.

In the Nordic Seas and Arctic Ocean potential vorticity contours $q = f/H$ (where H is water depth) effectively coincide with isobaths because f is approximately constant. These f/H contours (Figure 7a) can be seen to close within basins (rather than being blocked by isobaths as typical of midlatitude ocean basins), and potential vorticity gradients (directed across isolines of f/H) are dominated by topographic slopes. One might expect that depth-integrated flow would have a proclivity to conserve q and thus follow bathymetry. This is schematized in Figure 8; idealized closed f/H contours (black) lie either entirely within the Arctic basins, or enclose both the Nordic Seas and the Arctic Ocean. These are the 'railway tracks' along which the barotropic flow circulates, as indicated by the arrows in Figure 8. The sense of the flow along f/H contours depends on the sign of the vorticity input, set by the wind-stress curl integrated over the area within the q contour in question.

Isachsen, LaCasce, Mauritzen, and Häkkinen (2003) exploited this idea to describe the time-varying depth-averaged Arctic Ocean and Nordic Seas circulation. They integrated the governing vorticity equation over an area bounded by a closed f/H contour and showed that the flow in the bounded region co-varies with the difference between transport in the wind-driven surface Ekman layer and the bottom Ekman layer. This is the barotropic mode excited by time-varying winds.

Nøst and Isachsen (2003) developed a related model for the local flow using an integrated vorticity balance in an area surrounded by an f/H contour, but for the time-mean bottom velocities of the Arctic Ocean and Nordic Seas. The steady-state balance between vorticity input and output is given by

$$\iint_A \nabla \times \boldsymbol{\tau_s} dA = \oint_C \boldsymbol{\tau_b} \mathbf{.dl}, \tag{7}$$

where $\boldsymbol{\tau_s}$ is the surface stress and $\boldsymbol{\tau_b}$ the bottom stress. This states that the surface vorticity input by the wind within q surfaces is balanced by bottom stress integrated around closed q contours. Relating the bottom stress to bottom velocity $\boldsymbol{v_b}$ through a linear drag law, $\boldsymbol{\tau_b} = -\rho_0 \mu \boldsymbol{v_b}$ (where μ is a linear friction parameter), (7) can be rearranged as

$$\boldsymbol{v_b} \approx -\frac{1}{\rho_0 \mu L} \iint_A \nabla \times \boldsymbol{\tau_s} dA \frac{|\nabla q|}{\frac{1}{L}\oint_C |\nabla q| dl}. \tag{8}$$

This says that the flow at any location along an f/H contour can be estimated as the product of the surface wind-stress curl $\nabla \times \boldsymbol{\tau_s}$ integrated over the area within the contour, divided by the length L of the $q = f/H$ contour, and the magnitude of the local slope relative to the average slope of the f/H contour. That is, the magnitude of the cross-stream vorticity gradient, $|\nabla q|$, modulates the strength of the bottom current by a factor $|\nabla q| / \left(\frac{1}{L}\oint_C |\nabla q| dl\right)$. Nøst and Isachsen (2003) show that (8) gives reasonable agreement with current-meter measurements of the bottom flow in the Arctic Ocean. Surface flows may then be computed from the bottom-velocity prediction (equation 8) using climatological hydrographic data to obtain thermal wind shear from the bottom to the surface. Note, however, that the presence of sea ice is not accounted for in estimates of surface-ocean stresses although in Section 7 we return to the role of sea ice as a control on ocean dynamics.

Considering each of the closed f/H contours plotted in Figure 7a, we compute the total area-integrated wind-stress curl within each contour (divided by the length of the contour), and plot it as a function of area enclosed by the contour (Figure 7, where the plotted points are colored by the depth of the f/H contour in question; see also Figure 13 of Nøst and Isachsen (2003)). The area-integrated wind forcing for f/H contours that enclose both the Nordic Seas and the entire Arctic Basin is cyclonic: comprised of contributions of strong cyclonic forcing in the Nordic Seas, and relatively weak anticyclonic wind forcing in the Canadian Basin. In this sense, the cyclonic Atlantic Water boundary current in the Canadian Basin is driven by the cyclonic atmospheric forcing in the Nordic Seas. This is the concept that flow following f/H contours is driven by *remote* wind stresses (outside the Arctic Ocean), while the balancing bottom drag is distributed throughout the Arctic basin. The concept is consistent with a recent climate model study that suggests intensified Atlantic Water inflow to the Nordic Seas and Arctic Ocean is related to a strengthening of the Icelandic Low (Årthun, Eldevik, & Smedsrud, 2019).

The interior anticyclonic flow in the Canada Basin (i.e., the Beaufort Gyre), around closed f/H contours entirely within the Canada Basin, is then also explained by the area-integrated anticyclonic wind forcing for closed contours in that region (Figure 7a,b). We note that these ideas are distinct from others that are based on an integral constraint of potential vorticity (e.g., Karcher, Kauker, Gerdes, Hunke, & Zhang, 2007; Yang, 2005), where if the net potential vorticity introduced to the Arctic basin via the strait inflows is positive (negative), the result is an interior cyclonic (anticyclonic) circulation; further, large buoyancy fluxes in the Barents Sea are an important source of potential vorticity.

5.2.1 Eddy influences

So far, we have only discussed a model in which energy dissipation is confined to the bottom boundary layer. Lateral eddy momentum fluxes, eddy-topography interactions and diapycnal fluxes have been neglected. It has been shown, for example, that lateral eddy momentum fluxes may be at least as important as bottom friction in balancing surface forcing (Dewar, 1998), much as synoptic eddy momentum fluxes maintain the surface wind patterns in the atmosphere. Dewar (1998) presents an analytical layered model of abyssal flow in the Atlantic (invoking area integration around closed f/H contours) in which eddy fluxes arising from baroclinic instability are parameterized as down-gradient potential vorticity diffusion (see Marshall, Jamous, & Nilsson, 2001), a generalization of thickness diffusion.

Applied to a 2-layer model forced by anticyclonic winds, wind-driven Ekman pumping in the upper layer is balanced by a divergent eddy mass flux in that layer. In the deep layer, eddy-driven flow mixes potential vorticity downgradient such that there are outward eddy potential vorticity fluxes over a bowl-shaped basin, and inward eddy potential vorticity fluxes over a seamount. These must be balanced by fluxes in the opposite sense in the bottom boundary; inward mass flux in the bottom boundary gives rise to a mean flow that tends to be cyclonic in the bowl case, and vice versa. In this way, a gyre can be set up in the deep layer, which is cyclonic around closed f/H contours in a deep basin and anticyclonic over a seamount, i.e., the direction of circulation in the deep layer depends on the bathymetry rather than the sign of the wind-curl forcing.

The applicability of this description to the Arctic's Atlantic Water circulation is unclear. The formalism would predict a cyclonic circulation in the deep Beaufort Gyre, whereas observations indicate that the deep flow is in the same direction (i.e., anticyclonic) as the upper-ocean circulation (e.g., Dosser & Timmermans, 2018). Furthermore, in the two-layer model within a bowl-shaped basin described above, a reversal with depth of the horizontal potential vorticity gradients is absent, yet is a necessary condition for baroclinic instability.

Lastly, with respect to eddy influences, it has been shown that accounting for eddy interactions with seafloor topography can give rise to a mean cyclonic circulation in a deep basin, a result referred to as the *Neptune Effect* (Holloway, 1992, 2004). The circulation results from the stress generated by eddy pressure anomalies correlated with seafloor slope. This effect is likely to influence propagation speeds and diffusion of the cyclonic Atlantic Water flow. For example, including a parameterization of the Neptune Effect in an ocean model yields an Arctic Ocean flow field that is more consistent with that inferred from tracer observations; the overall cyclonic flow is enhanced around individual basins, most intense over topographic boundaries (Nazarenko, Holloway, & Tausnev, 1998; I. Polyakov, 2001).

5.3 Estuary vs. f/H-following perspectives

We have analyzed the processes driving the circulation of Atlantic Water into and around the Arctic Ocean basin. Both the estuary model invoking diabatic processes, and the f/H-following wind-driven model that invokes dynamical forcing by the winds, provide important perspectives. Diabatic processes must play an essential role because Atlantic Water flowing in to the Arctic has its properties changed as it circuits the basin: surface buoyancy forcing, a range of mixing mechanisms and eddy stirring all play a role. Furthermore, winds through cyclonic curl forcing over the Nordic seas set the sense of circulation around f/H contours and orchestrate the gateway into the Arctic. Both wind- and buoyancy-driven processes work together to facilitate Atlantic Water inflow and circulation around the Arctic, processes that do not depend on the strength and structure of the AMOC. It remains unclear how this concept relates to modeling studies. Delworth et al. (2016) examine climate model output to deduce a positive relationship between AMOC strength and ocean heat transport into the Barents Sea, where they attribute AMOC fluctuations to changes in the North Atlantic Oscillation. Other climate model studies find this same result for internal climate variability, but suggest the opposite result under climate change (greenhouse gas forcing): ocean heat transport to the Nordic Seas and Arctic increases at the same time as the AMOC weakens (Årthun et al., 2019; Oldenburg, Armour, Thompson, & Bitz, 2018). No doubt feedbacks on the regional atmospheric circulation (e.g., the Icelandic Low) are also important.

Co-existing with the arterial Atlantic Water flow are relatively cold, fresh, wind-driven surface-intensified patterns in the interior Arctic basins: the Transpolar Drift Stream and the Beaufort Gyre. In the model of Nøst and Isachsen (2003), the prevailing anti-cyclonic winds set up the anticyclonic Beaufort Gyre circulation in the Canadian Basin (see magenta contours in Figure 7a), and bottom friction provides the balance to the wind-stress curl. The role of bottom friction and topographic influences on the Beaufort Gyre (which can at times be centered over the Canada Basin's abyssal plain) and Transpolar Drift Stream dynamics are less obvious; the circulation is surface intensified in these strongly-stratified, wind-driven systems. We now outline some of the essential features of the Transpolar Drift Steam, before moving on in Section 7 to review the present state of understanding of Beaufort Gyre dynamics.

6 The Transpolar Drift Stream

The Transpolar Drift Stream of ice and water flows from the Siberian Shelf towards Greenland and the Nordic Seas, as is evident in the wind and sea-ice fields shown in Figures 2a and c. Many studies have addressed the sea-ice drift component of the Transpolar Drift Stream, readily monitored by remote sensing and drift of floe-tracking buoys (e.g. Kwok, 2009; Rigor, Wallace, & Colony, 2002; Serreze, McLaren, & Barry, 1989). The strength and orientation of the Transpolar Drift Stream is associated with the relative domains and intensity of the Beaufort High and Icelandic Low pressure systems. During conditions of a weakened Beaufort High, and deepened Icelandic Low, ice drifts cyclonically in the Eurasian Basin, transiting from the Laptev Sea towards the Canadian Basin before drifting towards Fram Strait (Kwok, Spreen, & Pang, 2013). A stronger Beaufort High, characterized by an expanded anticyclonic circulation, and a weaker Icelandic Low, are associated with a more direct path from the Laptev Sea to Fram Strait of ice drift in the Transpolar Drift Steam (e.g., Kwok et al., 2013).

The geostrophic ocean flow is aligned with the sea ice Transpolar Drift Stream in the vicinity of the front between relatively warm and fresh surface waters, associated with the northern extent of the Beaufort Gyre, and colder, saltier surface waters that comprise the Transpolar Drift Stream (see Figure 3a, the confluence of contours at the northern boundary of the Beaufort Gyre, and aligned with the Transpolar Drift Stream) (Morison, Steele, & Andersen, 1998; Morison, Steele, Kikuchi, Falkner, & Smethie, 2006; Steele et al., 2004). This surface front also bounds the northern extent of Pacific Water influence in the upper halocline (F. McLaughlin, Carmack, Macdonald, & Bishop, 1996; Morison et al., 1998), and is a region of water mass exchange owing to frontal baroclinic instability (Timmermans, Toole, Proshutinsky, et al., 2008). Currents in the upper 20 m of the water column are around 6 - 10 cm s^{-1} (e.g., Armitage et al., 2017), suggesting the transport of water from the Siberian shelf to Fram Strait takes approximately one year.

The position of the Atlantic-Pacific boundary has been observed to be in the vicinity of the Lomonosov Ridge to as far south as the Mendeleyev Ridge separating the Canada and Makarov basins (Boyd, Steele, Muench, & Gunn, 2002; Morison et al., 1998; Steele & Boyd, 1998). Positional changes have been attributed to changes in large-scale wind forcing patterns which re-direct freshwater inputs from Siberian rivers and shift the axis of the Transpolar Drift Stream (Boyd et al., 2002; Morison et al., 1998; Steele & Boyd, 1998; Timmermans et al., 2011); the shift is schematized in Figure 4 of Morison et al. (2012). Further complicating this general picture and the spatial distribution of surface freshwater and circulation patterns may be the fact that a weakened Beaufort Gyre allows for fresh water release (Timmermans et al., 2011). This is explored further in Section 8.

Timescales of ocean baroclinic adjustment to atmospheric forcing changes over the central Arctic are uncertain. Morison et al. (2006) considers atmospheric forcing in context with annual hydrographic measurements in the central Arctic Ocean to infer the timescale of the response of the upper ocean to large-scale atmospheric circulation changes is around 3 to 7 years. These adjustment timescales are influenced by processes balancing momentum input by the winds, mediated by sea-ice cover. We describe these processes as they control Beaufort Gyre dynamics in the next section.

7 The Beaufort Gyre

The anticylonic Beaufort Gyre, with a diameter around 800 km, dominates the Canadian Basin circulation. It is characterized by typical speeds in the upper water column of several cm/s (McPhee, 2013; B. Zhao & Timmermans, 2018); water parcels at the gyre periphery take roughly 2 years to complete a revolution. The Beaufort Gyre has been much more intensively studied than the Transpolar Drift Stream, in part because it is the largest reservoir of fresh water in the Arctic Ocean (e.g., L. K. Coachman, 1969; A. Proshutinsky, Dukhovskoy, Timmermans, Krishfield, & Bamber, 2015; A. Y. Proshutinsky & Johnson, 1997; Worthington, 1953). The presence of upper-ocean fresh water allows for the persistence of sea ice because the associated stratification acts as a barrier to upward heat transport (e.g., Aagaard, Coachman, & Carmack, 1981). Further, the release of Beaufort Gyre fresh water may affect climate dynamics in the North Atlantic by changing the stratification there (e.g., Belkin, Levitus, Antonov, & Malmberg, 1998). Mixed-layer salinities are freshest in the Beaufort Gyre center, the result of surface Ekman convergence of fresh water deriving from river discharge, net precipitation and sea-ice melt, and there is a surface gradient towards higher salinities away from the center (Figure 2a). The Beaufort Gyre center (characterized by a maximum in sea-surface height and maximum depth of halocline density surfaces, Figures 3, 9 and 10) generally coincides with the atmospheric Beaufort High center and its intensity is associated with the strength of the wind-stress curl, Figure 2c (e.g., Armitage et al., 2017; L. K. Coachman, 1969; A. Proshutinsky et al., 2009; A. Y. Proshutinsky & Johnson, 1997).

Related to the accumulation and release of Beaufort Gyre fresh water, A. Y. Proshutinsky and Johnson (1997) put forward that there are two regimes of atmospheric circulation over the Arctic Ocean – one in which the Beaufort High atmospheric pressure dominates (an anticyclonic regime), and the other in which the Icelandic Low pressure system is expanded and dominates (a cyclonic regime). These regimes shift from one to another on a timescale of around 5 - 7 years, although the precise mechanism for this shift is unclear (A. Proshutinsky et al., 2015). Observations and numerical experiments suggest that during an anticyclonic regime, the Beaufort Gyre accumulates fresh water, and during a cyclonic regime, it can be released to exit the Arctic Ocean into the North Atlantic (A. Proshutinsky, Bourke, & McLaughlin, 2002). Only since the early 2000s have we had sufficient year-round observations of the coupled atmosphere-ice-ocean system to build up a deeper understanding of the relationships between atmospheric forcing and Beaufort Gyre fresh water. For example, the accumulation of fresh water requires the availability of fresh water (e.g., sea-ice melt water or river influxes) to coincide with atmospheric forcing that drives Ekman convergence in the surface ocean layer. A. e. a. Proshutinsky (2019) show that the dominant contributions to recent fresh water accumulation in the Beaufort Gyre have been Pacific Water inflows through Bering Strait and fresh water from the Mackenzie River; changes to either could yield changes in Beaufort Gyre fresh water content even while the atmospheric forcing remains the same. We re-visit changes in Beaufort Gyre fresh water in Section 8.

7.1 Potential vorticity and ventilation

The field of potential vorticity is useful for understanding the large-scale circulation of the Beaufort Gyre. Just as low Rossby number barotropic flow associated with the Atlantic Water is steered by f/H contours, the flow on density surfaces in the Beaufort Gyre's stratified halocline follows f/h contours where h is the vertical distance between two density surfaces whose density difference is $\delta\sigma$. We then define the potential vorticity $q = (\delta\sigma/\rho_0)(f/h)$. The possible geometry of q contours is shown schematically in Figure 8 (blue contours). A closed q contour suggests that water can circulate around the contour without having its potential vorticity reset. If, instead, q contours thread back to density outcrops at the surface, ventilation is possible in which fluid flowing along these contours enters/exits the halocline from/to the surface mixed-layer. In this way, inspection of the field of potential vorticity allows one to distinguish between waters that are relatively isolated from the surface and those that are ventilated.

We select the layer defined by $\sigma = 25-27.4$ kg m^{-3} to represent the main halocline (Figure 3b,c). In the central basins its top surface is consistently below the mixed layer so that it is not subject to seasonally-varying surface buoyancy and wind forcing (Figure 9a). The layer is characterized by a potential vorticity minimum in the central Beaufort Gyre, and a potential vorticity maximum (higher stratification, a consequence of surface Ekman transport towards the Beaufort Gyre) approximately paralleling the Lomonosov Ridge at the front between Canadian and Eurasian Basin water, i.e., the Atlantic-Pacific boundary described in Section 6 (Figure 9b). The outcrop of the layer can be seen at the margins of the Beaufort Gyre, where there is a surface front between saltier Chukchi Sea water and relatively fresh Beaufort Gyre water (see Figure 2a), and in the Eurasian Basin. We see that q contours in the halocline layer thread to the outcrop in the Chukchi Sea indicating ventilation (Figure 9b). This supports the idea that the halocline layer is ventilated by waters whose temperature and salinity properties are set at the surface. Timmermans, Marshall, Proshutinsky, and Scott (2017); Timmermans et al. (2014) argue that the Beaufort Gyre is ventilated by water that is transferred from the surface in the Chukchi Sea region down and laterally into the halocline by wind-driven Ekman pumping and the large-scale geostrophic circulation. The process is analogous to mid-latitude thermocline ventilation (e.g., Iselin, 1939; Luyten, Pedlosky, & Stommel, 1983; H. M. Stommel, 1979). In this way Pacific Water is swept into the Beaufort Gyre such that it penetrates and ventilates the entire interior Canada Basin halocline where Pacific Water layers reside beneath the surface mixed layer (see Timmermans et al., 2014).

As a consequence of its ventilation, the halocline of the Beaufort Gyre is characterized by two stratification maxima (Figures 3b and 10c). The first and shallowest corresponds to the mixed-layer base and is maintained by sustained surface Ekman convergence of fresh water. The second peak in the stratification around 200 m depth is at the base of the Pacific Winter Water Layer (Figure 10b,c), and is thought to originate at the surface in the Chukchi Sea and ventilate the region in winter (Timmermans et al., 2017, 2014). Deeper down, waters from the cyclonic Atlantic Water boundary current are carried into the interior of the Canada Basin by thermohaline intrusions and eddies (F. A. McLaughlin et al., 2009). Below the Atlantic Water Layer, the deep and bottom waters share the same large-scale circulation patterns, although are much weaker in strength than the overlying anticyclonic circulation (see Dosser & Timmermans, 2018; B. Zhao & Timmermans, 2018).

There is a vast store of available potential energy in the Beaufort Gyre halocline that is susceptible to baroclinic instability. The basic state isopycnals indicate a change in sign with depth of the horizontal potential vorticity gradient satisfying the necessary criterion for baroclinic instability (Figure 10d). If the planetary potential vorticity gradient is negligible, the sign of the interior meridional background potential vorticity gradient may be determined by the sign of the meridional isopycnal layer thickness gradient. In the schematic representation of the Beaufort Gyre, the horizontal potential vorticity gradient changes sign between the layers shown, indicating how the gyre may be baroclinically unstable (Figure 10d). The observed energetic eddy field (Figure 10e) and predicted scales and growth rates (Section 4.2 and Figure 4) suggest that the gyre is indeed baroclinically unstable, with important implications for its dynamics, as we now discuss.

7.2 Fundamental dynamics of the Beaufort Gyre

Fundamental dynamics of the Beaufort Gyre differ from mid-latitude wind-driven gyres which are characterized by a Sverdrup interior and frictional balance at western boundary currents (Munk, 1950; H. Stommel, 1948). It appears that the dynamics of the Beaufort Gyre has much in common with the dynamics of the Antarctic Circumpolar Current (ACC). Meridional barriers are also absent in the Southern Ocean and mesoscale eddy transfer is key to satisfying large-scale budgets of the ACC (see Marshall & Radko, 2003). Residual-mean theory is central to understanding the dynamics of such systems.

7.2.1 Residual-mean theory

We consider the Beaufort Gyre as a system in which the prevailing winds pump fresh water in to the interior of the gyre, thickening halocline layers. This process is balanced by mesoscale eddy fluxes (i.e., bolus fluxes) that reduce thickness variations. The total transport in an isopycnal layer (due to the mean flow $\overline{\mathbf{v}}$ plus transport by eddies) is known as the residual-mean (as reviewed by, e.g., Andrews, Leovy, & Holton, 1987) defined by

$$\underbrace{\frac{\overline{\mathbf{v}h}}{\bar{h}}}_{\text{Residual-mean}} = \underbrace{\overline{\mathbf{v}}}_{\text{Eulerian-mean}} + \underbrace{\frac{\overline{\mathbf{v}'h'}}{\bar{h}}}_{\text{Eddy-induced transport}} , \tag{9}$$

where h is the thickness of a density layer, overbars denote an average and primes departures from that average. The residual-mean transport through a layer has a component in addition to the Eulerian mean because there can be correlations between the lateral flow and the thickness of the layer, leading to a significant bolus transport, $\overline{\mathbf{v}'h'}$. In the ACC, for example, bolus fluxes are significant and residual and Eulerian transports differ greatly from one-another, a fact that has fundamental implications for our understanding of its dynamics (see the review by Marshall & Speer, 2012). This is also true for the Beaufort Gyre (G. E. Manucharyan, Spall, & Thompson, 2016; Meneghello et al., 2017; Yang, Proshutinsky, & Lin, 2016).

Meneghello et al. (2017) show that observations are consistent with the large-scale wind-driven Ekman transport integrated over the Beaufort Gyre being largely balanced by eddy fluxes (i.e., the left hand side of equation (9) is a residual of the terms on the right hand side which tend to cancel one-another). They consider the zero residual-mean limit (analogous to studies to understand Southern Ocean dynamics, e.g., Marshall & Radko, 2003) and test whether the Eulerian-mean circulation can balance the bolus transport by eddies. Introducing an eddy diffusivity K_D to characterize eddy transport (as in Gent & Mcwilliams, 1990), a zero residual-mean balance yields

$$K_D = \frac{1}{\rho_0 f_0} \frac{\iint \nabla \times \boldsymbol{\tau_s} dA}{\iint \nabla^2 h dA}, \tag{10}$$

where $h(r)$ refers to the depth of an isopycnal in the stratified Beaufort Gyre, and $\boldsymbol{\tau_s}$ is the stress on the surface ocean, influenced by the presence of sea-ice cover (we discuss the role of sea ice shortly). The integrals are over an area enclosed by a particular geopotential height contour in the (r, z) plane. The numerator of (10) represents the area integrated Ekman pumping and the denominator can be considered as the balancing thickness flux. As described in Section 4.2, mooring measurements of velocity in the Beaufort Gyre allow for observational estimates of K_D invoking a mixing length theory. The magnitude and vertical structure of these estimates are in rough agreement with values inferred from (10) as shown by Meneghello et al. (2017). This suggests that in the Beaufort Gyre, eddy fluxes may be sufficient to balance Ekman pumping leading to a small residual-mean flow. We note that (10) yields the scaling for the depth of the halocline:

$$h \sim \frac{R\tau_s}{\rho_0 f_0 K_D}, \tag{11}$$

where R is an estimate for the radius of the gyre. Taking typical values for these parameters ($R = 400$ km, $\tau_s = 0.5 \times 10^{-2}$ N m^{-2}, $f = 10^{-4}$ s^{-1}, and $K_D = 400$ m^2 s^{-1}), gives $h \approx 50$ m, broadly in accord with the depth scale of the upper halocline and Figures 3c and 10c (see e.g., Meneghello et al., 2017). This is the same as the scaling for the vertical scale of the ACC discussed by Marshall and Radko (2003) and the same dynamics are at work.

The axisymmetric model described above, although highly instructive, cannot capture important asymmetries induced by topographic effects. Notably, the west side of the southern Canada Basin is bounded by the steep Northwind Ridge; the ridge has a slope of more than 10 degrees in places from the abyssal plain of the Canada Basin (around 3800 m deep) to the Chukchi Borderland and Northwind Abyssal Plain regions, shallower than 1000 m in parts (Jakobsson et al., 2008, 2012). This prominent topographic feature may affect the symmetry of the gyre, and its susceptibility to baroclinic instability (e.g., G. Manucharyan & Isachsen, 2019).

7.2.2 Wind forcing mediated by sea ice

In the absence of sea ice there is a direct relationship between the wind-stress acting on the ocean and the associated Ekman pumping. In the presence of sea ice, however, wind applies stress to the ice which, less the lateral stresses within the ice, applies stress to the ocean. Moreover, the strength and sign of Ekman pumping in the surface ocean can be influenced by geostrophic ocean currents moving against the sea ice (Dewey et al., 2018; Meneghello, Marshall, Campin, Doddridge, & Timmermans, 2018; Meneghello, Marshall, Timmermans, & Scott, 2018). Consider, for example, a situation in which the Arctic Ocean is almost completely ice covered in winter and internal lateral stresses in the ice pack are sufficiently large that the sea-ice motion in response to the prevailing anticyclonic wind forcing is small. At the same time, there is a persistent ocean geostrophic flow of the anticyclonic Beaufort Gyre acting against the near-motionless sea ice. This gives rise to Ekman divergence in the surface ocean layer and upwelling from the interior. Meneghello, Marshall, Timmermans, and Scott (2018) show that this upwelling each winter greatly reduces the annual cumulative Ekman downwelling from the value it would have had in the ice-free case; observations of ocean geostrophic flow, winds and sea-ice drift indicate that cumulative Ekman downwelling can be up to 80% lower than an inferred value that neglects the presence of ice. Meneghello, Marshall, Campin, et al. (2018) describe how this effect acts as a self-regulator, which they call the *ice-ocean stress governor*, and which sets the speed of the Beaufort Gyre. As the gyre increases in speed in response to sustained anticyclonic wind forcing, and/or sea-ice drift slows in winter when internal ice stresses increase, ocean currents ultimately reach ice speeds and the surface stress on the ocean shuts off. In this way, the ice-ocean stress governor can equilibrate the gyre, which implies a limit on freshwater accumulation. This is another example of the internal system dynamics arranging to "turn off" the residual flow and the forcing thereof. The implications for the future Arctic, where ice will likely be absent in summer and more mobile in winter, are discussed in the next section.

8 Arctic Ocean variability, climate change and future perspectives

The rapid changes that are underway in the Arctic compel an assessment of how Arctic Ocean dynamics might fundamentally change in the future. One conspicuous scenario to consider is a seasonally ice-free Arctic Ocean, with no sea ice for part of the summer/fall and a thinner sea-ice pack in winter/spring. How will Arctic oceanography be different in this regime? Here, we contemplate two aspects of such a change; the first relates to ocean heat and the second relates to fresh water and energetics of the large-scale circulation.

8.1 Changing ocean heat

In recent decades, a general warming of the upper Arctic Ocean has been widely documented in observations (e.g., E. Carmack et al., 2015; I. V. Polyakov et al., 2017; Timmermans, Toole, & Krishfield, 2018). Linear trends indicate summer mixed-layer temperatures increasing at about 0.5°C per decade over 1982-2018 in large areas of the Arctic Ocean that are ice-free in summer (Timmermans & Ladd, 2019). Increasing mixed-layer temperatures predominantly result from increased summertime solar absorption into the surface ocean that is associated with sea-ice losses and decreased Arctic Ocean albedo; the ice-albedo feedback mechanism has been a dominant factor of recent sea-ice losses (D. K. Perovich & Richter-Menge, 2009). Further, the heat absorbed by the surface ocean has implications that persist beyond the melt season. Timmermans (2015) showed that in the Canadian Basin, the excess heat absorbed by the surface ocean can lead to sea ice that is 25% thinner at the end of the growth season. Similar estimates apply for the region to the northeast of Svalbard, where observations indicate a delayed onset of freezing that follows excess solar absorption by the oceans (Ivanov et al., 2016).

Ocean heat advected from the Pacific Ocean is also increasing, and has been implicated in triggering the ice-albedo feedback mechanism in the Chukchi Sea (Woodgate et al., 2010), which has experienced the fastest rate of sea-ice decline in the entire Arctic Ocean (Comiso, 2012; Serreze, Crawford, Stroeve, Barrett, & Woodgate, 2016). Heat transport from the Pacific Ocean through Bering Strait increased by 60% over 2001-2014, from around 10 TW in 2001 to 16 TW in 2014; this was attributed to increases in both volume flux and temperature (Woodgate, 2018; Woodgate, Stafford, & Prahl, 2015).

Some of the additional ocean heat in the Chukchi Sea, that derives both from excess solar absorption as a consequence of reduced sea-ice cover, and increased advection from the Pacific Ocean, is accumulated and stored within the Beaufort Gyre halocline, away from the influence of surface-ocean buoyancy fluxes and wind-driven mixing. As described in Section 7.1, anomalously warm waters at the surface in the Chukchi Sea are saltier (and therefore more dense) than the fresher, cooler waters at the surface in the interior Beaufort Gyre, and there is a surface front between the two water types (approximately at the $\sigma = 25$ kg m^{-3} outcrop in the southwest Beaufort Sea, see Figure 9); the denser (warmer) water type ventilates the Beaufort Gyre halocline. In the interior Beaufort Gyre, Pacific Water Layer maximum temperatures increased by about 0.5°C between 2009 and 2013 (Timmermans et al., 2014), and integrated heat content in the warm Pacific Water Layer approximately doubled over the period 1987-2017 (Timmermans, Toole, & Krishfield, 2018). The amount of additional heat is enough to melt almost 1 m of sea ice should it escape to the surface. Understanding the fate of this heat is the subject of ongoing research.

It may be expected that under seasonally ice-free conditions (i.e., open water for longer duration each summer in the Chukchi Sea), intensified solar absorption by the ocean should continue, and therefore stored ocean heat should increase. On the other hand, a different scenario may unfold. Ventilation of the Beaufort Gyre halocline relies on the presence of the surface front (where the density contrast exists because of the salinity differences) between Chukchi Sea waters and Beaufort Gyre waters. At present Arctic Ocean temperatures, the coefficient of thermal expansion α is small and temperature has a negligible effect on density. Therefore, although the summertime surface Chukchi Sea waters are several degrees warmer than the Beaufort Gyre surface waters, the saltier Chukchi Sea surface waters are more dense than those of the Beaufort Gyre, and the summertime solar-warmed water can continue to ventilate the Beaufort Gyre halocline. However, as warming continues, α will increase, and temperature will have an increasingly important influence on the density as it does in the mid-latitude oceans characterized by a thermocline. A possible future scenario is that the warming of the Chukchi Sea waters will be sufficiently strong as to have a compensating effect on the salinity differences on density, and the front will be eliminated (Timmermans & Jayne, 2016). This would shut off the Beaufort Gyre halocline ventilation, and the mechanism for the accumulation of ocean heat, during the warmest periods.

8.2 Atlantification of the Arctic

The concept and implications of water-mass types in the polar region becoming closer to those characterizing mid-latitude oceans has also been explored on the Atlantic Ocean side of the Arctic. Mean Atlantic Water temperatures at Fram Strait and the Barents Sea Opening increased by around 1-1.5°C from 1980-2012 with long-term trends in volume inflow estimates difficult to infer given observation limitations (Muilwijk, Smedsrud, Ilicak, & Drange, 2018). Recent changes in the vicinity of the Atlantic Water inflow to the Arctic Ocean, including reduced sea ice, weaker stratification and enhanced Atlantic Water Layer heat fluxes further northeast into the Eurasian Basin, have been referred to as the *Atlantification* of the Arctic Ocean (Årthun, Eldevik, Smedsrud, Skagseth, & Ingvaldsen, 2012; Lind, Ingvaldsen, & Furevik, 2018; I. V. Polyakov et al., 2017). In the Eurasian Basin, vertical heat fluxes from the Atlantic Water Layer were estimated to be around 2-4 times larger in the 2014-2015 period compared with 2007-2008 (I. V. Polyakov et al., 2017).

The Atlantification concept alludes to the possibility of a northward progression of the warm α-oceans – North Atlantic water masses encroaching on the Arctic Ocean. At latitude around 45°N in both the North Pacific and Atlantic, there is a transition from an upper ocean that exhibits α stratification to a β stratification at the subarctic frontal zone, where warmer, saltier surface waters to the south meet cooler, fresher surface waters to the north (Roden, 1970, 1991), Figure 1b. The exact position of the subarctic front is related to the wind field, with the front in the vicinity of the maximum Ekman transport convergence (Roden, 1991). While the North Atlantic subarctic front covers a much broader range of latitudes, in both the Pacific and Atlantic oceans this $\alpha - \beta$ boundary, where the local surface density is maximal, is characterized by temperatures around 10°C (see e.g., Belkin & Levitus, 1996; E. C. Carmack, 2007), Figure 1b. Cabbeling, a process of sinking where two water masses of the same density but differing temperature and salinity mix and become more dense, is active in this frontal boundary region (see Garrett & Horne, 1978).

As mentioned in Section 3, the $\alpha - \beta$ stratification boundary is of importance to climate in that it establishes the southern extent of winter sea ice cover. Sediment core proxy data suggest significant changes in the position of the subarctic front over the Holocene period (Moros, Jansen, Oppo, Giraudeau, & Kuijpers, 2012; Perner et al., 2018), and much further back in the climate record, where the shifting influence of Atlantic and Polar Water types is related to changes in sea-ice extent (e.g., Stein, Fahl, Gierz, Niessen, & Lohmann, 2017). During the last major interglacial period (∼130,000 and 80,000 years ago, characterized by conditions warmer than today), Arctic sea ice biomarker proxy records and modeling suggest the Barents Sea was ice free for much of the year under the strong influence of inflowing Atlantic Water (Stein et al., 2017). The Barents Sea has been an increasingly dominant region of winter sea-ice loss in recent decades, largely resulting from increased Atlantic Water heat transport into the region (Smedsrud et al., 2013).

Climate model ensemble means (under continued increasing emissions) show a sustained incursion of Atlantic Water (marked by contours of the 1°C isotherm at 200 m depth, their Figure 12) from its present location in the vicinity of Fram Strait and the northern Barents Sea to almost paralleling the Lomonosov Ridge in the 2070s such that warm Atlantic Water fills the entire Eurasian Basin (Årthun et al., 2019). The main effect of this is a decrease in winter sea-ice thickness, by around 1.2 m between the 2010s and 2070s; average ocean-to-ice heat fluxes increase from around 0.5 W m^{-2} to 5 W m^{-2} in the Eurasian Basin between these two time periods. Increased Atlantic Water influence is likely to be a major player in the march towards a seasonally-ice-free Arctic Ocean. A potentially relevant feedback is increased mixing within the Arctic (discussed next) driving increased Atlantic Water influxes.

8.3 Sea-ice loss and ocean mixing levels

The loss of sea ice is not only linked to a build-up of ocean heat in the Arctic (and the indirect dynamical effects of this) – sea-ice loss has direct dynamical influences on the ocean as well. First, as implied in Section 4, wind-driven momentum input and therefore mixing levels are expected to increase under continued sea-ice losses and the absence of the buffering effects of sea-ice cover. While no studies have shown an increasing trend in Arctic Ocean mixing levels (it may be that sufficient data are not yet available), future conditions may be generally surmised from findings of more energetic inertial motions in the upper water column when sea-ice concentrations are lower (e.g., Plueddemann, Krishfield, Takizawa, Hatakeyama, & Honjo, 1998) and mooring observations that indicate upper water-column inertial wave energy levels in the absence of sea ice can be as large as mid-latitude levels (Rainville & Woodgate, 2009). Increased mixing will drive larger vertical heat fluxes (D'Asaro & Morison, 1992), causing further sea-ice melt. On the other hand, it may be that increased wind-driven momentum input does not lead to higher mixing levels because sea-ice losses are concurrent with increased halocline stratification.

Stratification increases, linked to freshening of the surface ocean (where fresh water originates from river influxes, land-ice melt, net precipitation, sea ice growth/melt, and northwards advection of mid-latitude waters), can inhibit convective and shear-driven mixed-layer deepening and suppress turbulent diapycnal diffusivities in the halocline. These processes regulate vertical heat transfer between the ocean interior and the surface. Arctic Ocean mixed-layer depths are typically around 25 to 50 m in winter and around 5-30 m in summer (e.g., Peralta-Ferriz & Woodgate, 2015; J. M. Toole et al., 2010). Between 1979 and 2012, central Arctic Ocean observations indicate a mixed layer shoaling of 0.5 to 1 m yr^{-1} (Peralta-Ferriz & Woodgate, 2015). Complicating the inferred consequences of this, Rainville, Lee, and Woodgate (2011) point out that the presence of thinner mixed layers can lead to more effective wind-driven momentum transfer to the ocean layers below; faster mixed-layer currents are generated if the same energy input is distributed over a thinner layer.

In recent decades, the margins of the Arctic Ocean (e.g., the East Siberian, Laptev, Chukchi, Kara and Barents seas) have seen freshwater decreases (Armitage et al., 2016). For example, freshwater content in the top 100 m of the northern Barents Sea decreased by about 32% between 1970-1999 and 2010-2016 (Lind et al., 2018). Mixed-layer deepening trends have been observed in these marginal regions in the past few decades, attributed to winds driving surface fresh water offshore (Peralta-Ferriz & Woodgate, 2015), and weakening stratification associated with Atlantification (I. V. Polyakov et al., 2017). The state of halocline strength and structure, and therefore mixing levels, in the coming decades will depend on the combined evolution of fresh water availability and its dynamical redistribution by winds modified to varying degrees by sea ice depending on season and region.

8.4 Changes in fresh water storage

Over 1992 to 2012 Arctic Ocean total freshwater content (integrated fresh water relative to a salinity of 34.8) has been increasing at a rate of around 600±300 km^3 yr^{-1}; about two-thirds of this trend has been attributed to salinity decreases, while the remaining third is a result of a thickening of the freshwater layer (E. C. Carmack et al., 2016; T. W. N. Haine et al., 2015; Rabe et al., 2014). The most comprehensive in-situ hydrographic measurements are from the Beaufort Gyre region where observations indicate total freshwater content has increased by almost 40% since the 1970s (from around 17×10^3 km^3 to 23.5×10^3 km^3 in 2018) (A. Proshutinsky, Krishfield, & Timmermans, 2019; A. e. a. Proshutinsky, 2019). Freshwater increases are associated with the strengthening of the Beaufort Gyre under the strong dominance of anticyclonic wind forcing over the Canadian Basin, freshwater accumulation from sea ice melt, increasing freshwater flux through Bering Strait and greater influence of McKenzie River water (R. A. Krishfield et al., 2014; A. Proshutinsky et al., 2015; A. e. a. Proshutinsky, 2019).

Anticipating the fate of Arctic fresh water as it is influenced by, and influences, sea-ice losses (via setting the stratification and regulating wind-energy input) is a priority for future climate projections. In the present-day Beaufort Gyre subject to sustained wind forcing, it is likely that both eddy fluxes and the ice-ocean stress governor play a role in equilibrating the gyre and its freshwater content. A future, seasonally ice-free Beaufort Gyre, with a corresponding thinner, more mobile winter sea-ice pack, would be characterized by a much less effective ice-ocean stress governor. Recent increases in Beaufort Gyre freshwater content may in part already be a manifestation of a less effective ice-ocean stress governor under recent sea-ice losses. Anticyclonic wind forcing balanced only by eddy fluxes will likely yield an equilibrium freshwater content that is larger, with a deeper halocline. That said, the new equilibrium may be uncertain given the changing fresh water availability (e.g., increased net precipitation, see Vihma et al., 2016) and topographic influences on gyre stability (that change with positional shifts in the gyre center).

Predicting future prevailing wind forcing is also a major source of uncertainty in understanding the fate of fresh water. A weakening of the Beaufort High and dominance of the Icelandic Low will support freshwater release, which may also be accompanied by a greater volume of Atlantic Water. For example, coupled modeling comparing the time periods 1979-88 and 1989-96 indicates a reduced Beaufort Gyre in the later period, a manifestation of a weakened Beaufort High and an expansion of the Icelandic low pressure system (Zhang, Rothrock, & Steele, 1998). Accompanying these changes is an increased penetration of Atlantic Water into the Arctic Ocean in the later period, and increased Polar Water outflow (i.e., an intensified East Greenland Current associated with fresh water release from the Beaufort Gyre). These changes are also documented in observations. Morison et al. (1998) analyze 1993 hydrographic observations that show increased influence of Atlantic Water/Eurasian Basin water types in the Arctic Ocean, with a shift in the position of the front between Eurasian Basin and Canadian Basin water types, which are characterized by fresher surface waters, Pacific Water influence and cooler Atlantic Waters. Consistent with a weakening of the Beaufort High and expanded influence of the Icelandic Low, the front shifts from its previous position around the location of the Lomonosov Ridge to a position roughly paralleling the Alpha and Mendeleyev Ridges; at the same time hydrographic measurements indicate a general warming of the Atlantic Water core temperatures. Morison et al. (1998) point out that the increased Atlantic sector influence (and reduced fresh water) in the Arctic Ocean persists for at least several years.

It may be that overall Arctic warming and sea-ice loss will lead to a reduced Beaufort High. A reversal of the prevailing anticyclonic circulation was documented in winter 2017, for example (Moore, Schweiger, Zhang, & Steele, 2018). This was attributed to warm surface air temperatures during the previous autumn, and reduced sea ice extents which generated an intensified low over the Barents Sea and increased cyclone propagation into the Beaufort Sea region (Moore et al., 2018). Such circulation patterns could become increasingly prevalent in a warming Arctic, which would have significant implications and feedbacks with respect to fresh water fluxes out of the Beaufort Gyre region.

9 A framework for interpreting Arctic Ocean circulation in a changing system, and future challenges

We have provided a general description of two distinct circulation patterns in the Arctic Ocean. Relatively warm and salty Atlantic waters enter through Fram Strait and the Barents Sea Opening, and circulate cyclonically around the Arctic basin boundaries and within Arctic sub-basins, ostensibly under strong topographic control. Co-existing with these arterial flows are wind-driven surface-intensified patterns driven interior to the Arctic – the Beaufort Gyre and the Transpolar Drift Stream. The ocean is capped by seasonally-varying sea-ice cover, with a distribution that is largely independent of topographic features. Pacific Ocean and river influxes further modify surface-water properties.

Both the estuary and f/H-following models for Atlantic Water circulation incorporate key essential processes, and on their own cannot provide a complete picture. In the estuary model, there is no role for topography within the Arctic Ocean and no allowance for winds to play a dynamic role. The simplest f/H-following model is barotropic, while strong stratification exists along the cyclonic pathway of the Atlantic Water. This is particularly true in the interior Canada Basin where stratification is strongest, eddies are active and flow is surface-intensified. Further, while bottom friction may be important, a complete model should take into account diabatic halocline mixing, lateral eddy fluxes, eddy pressure anomalies at the sea-floor slope, and under-ice stresses.

There are no-doubt complicated relationships between the arterial Atlantic Water and stratified Arctic Ocean interior flow. Coupled ice-ocean modeling, for example, suggests the Beaufort Gyre and Atlantic Water circulation can influence each other, e.g., an intensified Beaufort Gyre (under anomalously strong anticyclonic wind forcing) has been found to weaken and even reverse the Atlantic Water boundary current although the precise interactions remain unclear (Karcher et al., 2007). At least, the structure and water-mass properties of mesoscale eddies sampled within the Beaufort Gyre indicate efficient eddy fluxes from the Atlantic Water boundary current (and overlying Eurasian Basin halocline water types) to the Beaufort Gyre (Carpenter & Timmermans, 2012; M. Zhao & Timmermans, 2015).

We are building up a consistent description of the wind-driven Beaufort Gyre circulation and dissipation processes – both ocean-ice stresses and baroclinic eddy activity play key roles in balancing wind forcing – yet many open questions remain. One major understanding gap is that adjustment timescales for the Beaufort Gyre and upper-ocean response to wind forcing in the Eurasian Basin are not well known. These will be essential to constrain if we are to make viable assessments about how Beaufort Gyre will change with further sea-ice decline, the fate of freshwater, stratification and mixing processes, and how the fundamental dynamics will change with continued warming to a scenario where the dynamical influence of temperature will be more important.

Many gaps in our understanding exist because of the obstacles to acquiring sufficient measurements. While satellite remote sensing of ocean properties, including the meso- and smaller-scale flow field (and eddy kinetic energy) will continue to become more effective as sea ice declines, sea-ice cover will continue to remain an impediment for much of the year. Although sea ice can be a barrier to sustained remote and in-situ Arctic Ocean observing, sensors mounted in sea ice have provided invaluable measurements of the Arctic atmosphere-ice-ocean system (see the review by Timmermans, Krishfield, Lee, & Toole, 2018). However, there remain challenges of observing and quantifying ice-ocean stresses and eddy fluxes in the upper ocean, which we know to be critical in the dynamical balances. High spatial and temporal resolution measurements in the ice-ocean boundary layer are generally only possible through the use of sea ice as a platform from which to sample (and these are therefore Lagrangian measurements). Further, year-round measurements in the boundary layer are impracticable because seasonal sea-ice growth and dynamical ridging processes would compromise any sensors in the boundary layer. For this same reason, moored sensors must be placed deeper than a couple of tens of meters below the ice-ocean interface to avoid the possibility of being damaged by deep ice keels drifting past.

Year round measurement of the Arctic basin boundary regions (including its marginal seas) also remains a critical observational gap. As we have seen, these regions are characterized by the smallest flow scales and highest eddy kinetic energy. In addition, basin boundaries are the pathways for river influxes, Atlantic and Pacific inflows and boundary currents, and are the ocean regions with the strongest summertime solar warming. However, characterizing year-round dynamics and variability there is challenging for both political reasons (i.e., observing in Exclusive Economic Zones) and environmental reasons (i.e., ocean and sea-ice flows are exceptionally dynamic and destructive and exhibit strong seasonal variability). A range of observing approaches will be required to provide new observations in under-ice boundary layers and in the important basin margins – observations which will be vital to guide and constrain theoretical and modeling analyses to better understand the ocean's changing dynamical balances.

Acknowledgments

Support was provided by the National Science Foundation Division of Polar Programs under award 1603542. The Ice-Tethered Profiler data were collected and made available by the Ice-Tethered Profiler program (R. Krishfield, Toole, Proshutinsky, & Timmermans, 2008; J. Toole, Krishfield, Timmermans, & Proshutinsky, 2011) based at the Woods Hole Oceanographic Institution (http://www.whoi.edu/itp). Hydrographic climatology data are from the World Ocean Atlas 2018 (WOA18; https://www.nodc.noaa.gov/OC5/woa18/). Beaufort Gyre hydrographic data were collected and made available by the Beaufort Gyre Exploration Program based at the Woods Hole Oceanographic Institution (http://www.whoi.edu/beaufortgyre) in collaboration with researchers from Fisheries and Oceans Canada at the Institute of Ocean Sciences; Data are available online at http://www.whoi.edu/website/beaufortgyre/data.

References

Aagaard, K. (1981). On the deep circulation in the Arctic Ocean. *Deep Sea Research Part A. Oceanographic Research Papers*, *28*(3), 251–268.

Aagaard, K., & Carmack, E. C. (1989). The role of sea ice and other fresh water in the Arctic circulation. *Journal of Geophysical Research: Oceans*, *94*(C10), 14485–14498.

Aagaard, K., Coachman, L., & Carmack, E. (1981). On the halocline of the Arctic Ocean. *Deep Sea Research Part A. Oceanographic Research Papers*, *28*(6), 529–545.

Aagaard, K., Swift, J., & Carmack, E. (1985). Thermohaline circulation in the Arctic Mediterranean seas. *Journal of Geophysical Research: Oceans*, *90*(C3), 4833–4846.

Aksenov, Y., Ivanov, V. V., Nurser, A. G., Bacon, S., Polyakov, I. V., Coward, A. C., … Beszczynska-Moeller, A. (2011). The Arctic circumpolar boundary current. *Journal of Geophysical Research: Oceans*, *116*(C9).

Andrews, D. G., Leovy, C. B., & Holton, J. R. (1987). *Middle atmosphere dynamics* (Vol. 40). Academic press.

Armitage, T. W. K., Bacon, S., Ridout, A. L., Petty, A. A., Wolbach, S., & Tsamados, M. (2017). Arctic Ocean geostrophic circulation 2003-2014. *The Cryosphere Discussions*, *2017*, 1–32. Retrieved from `http://www.the-cryosphere-discuss.net/tc-2017-22/` doi: 10.5194/tc-2017-22

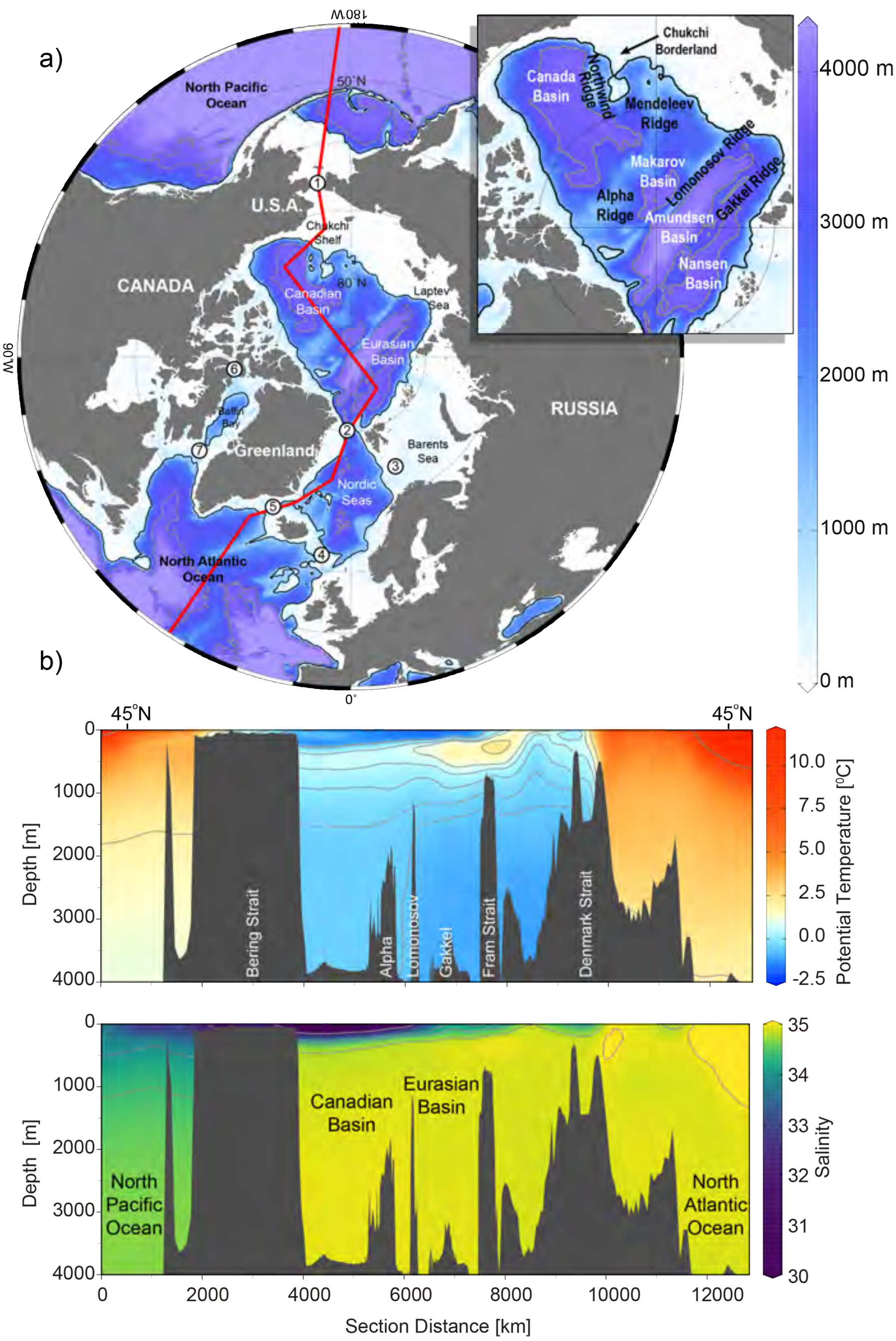

Figure 1. a) Map showing the main geographic features of the Arctic Mediterranean; the inset shows the Arctic Ocean in detail. 1000 m and 3500 m bathymetric contours are shown and numbers refer to 1. Bering Strait, 2. Fram Strait, 3. Barents Sea Opening, 4. Greenland-Scotland Ridge, 5. Denmark Strait, 6. Lancaster Sound, 7. Davis Strait. The red line marks the section shown in b) (top) Potential temperature (°C) and (bottom) salinity sections from the Pacific Ocean (left), through the Arctic Ocean to the Atlantic Ocean (right). Data are from the World Ocean Database (WOD18), all data in the period 2005-2017 (Boyer, 2018), compiled as the World Ocean Atlas (WOA18) (Garcia et al., 2019).

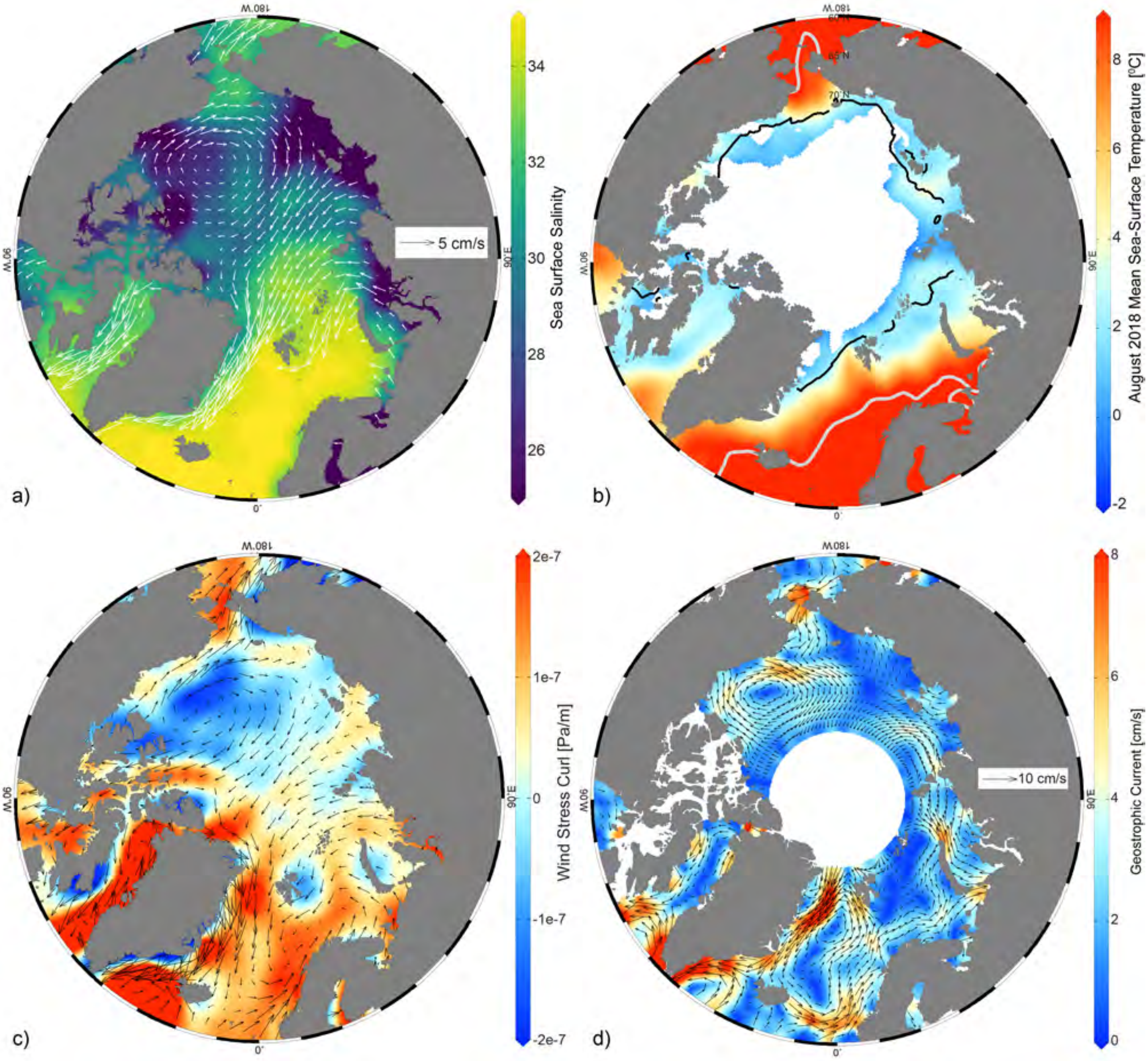

Figure 2. Maps of a) sea-surface salinity (WOD18, 2005-2017) [color] and March average sea-ice motion [white vectors] for the period 2005-17 from the Polar Pathfinder Daily 25 km EASE-Grid Sea Ice Motion Vectors data set available at the NASA National Snow and Ice Data Center Distributed Active Archive Center (Tschudi et al., 2016); b) August mean sea-surface temperature (°C) from the NOAA Optimum Interpolation (OI) SST Version 2 product (OISSTv2), which is a blend of in situ and satellite measurements (Reynolds et al., 2007); c) annual average surface wind stress [black vectors] and wind-stress curl (2005-17) [color] from NCEP/NCAR Reanalysis Monthly Means (Kalnay et al., 1996); d) Mean ocean geostrophic flow (cm/s) estimated for 2003-2014 from satellite-derived dynamic topography, where data are provided by the Centre for Polar Observation and Modelling, University College London (Armitage et al., 2017). In panel b), thick gray contours indicate the 10°C isotherm, white shading is the August 2018 mean sea ice extent, and the black line indicates the median ice edge for August 1982-2010. Sea ice extent data are from NSIDC Sea Ice Index, Version 3 (Fetterer et al., 2017).

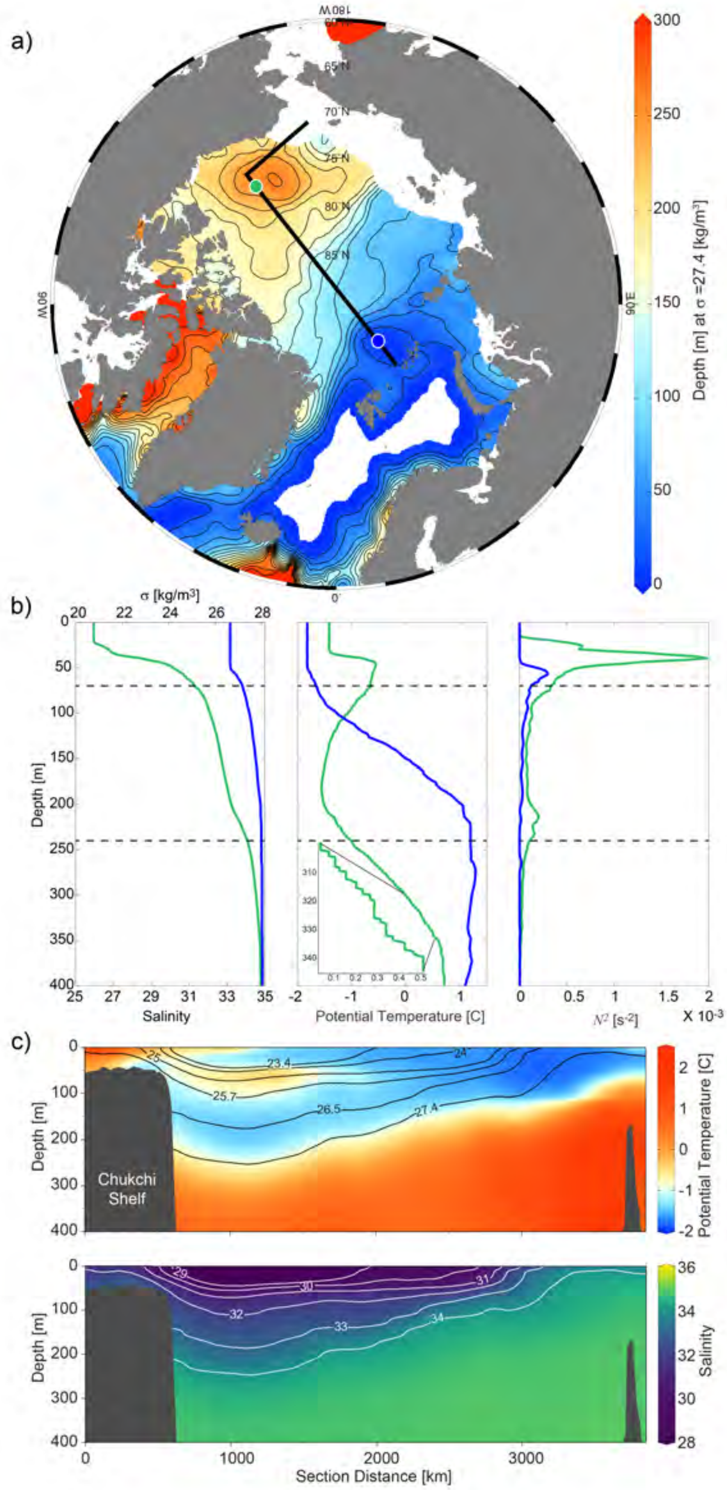

Figure 3. a) Depth of the σ=27.4 kg m^{-3} isopycnal. b) Example salinity, potential temperature (°C) and buoyancy frequency (N^2, s^{-2}) profiles from March 2010 in the Canada Basin (green profiles corresponding to the green marker in panel a) and Eurasian Basin (blue profiles, blue marker). The top x-axis in the left panel indicates the corresponding density and horizontal dashed lines mark the depths of σ=25 kg m^{-3} and σ=27.4 kg m^{-3} in the Canada Basin. The inset on the potential temperature profile shows the double-diffusive staircase structure. c) Sections of (top) potential temperature (°C) and (bottom) salinity from the Chukchi Sea (left) to the Eurasian Basin (right) along the black line shown in panel a).

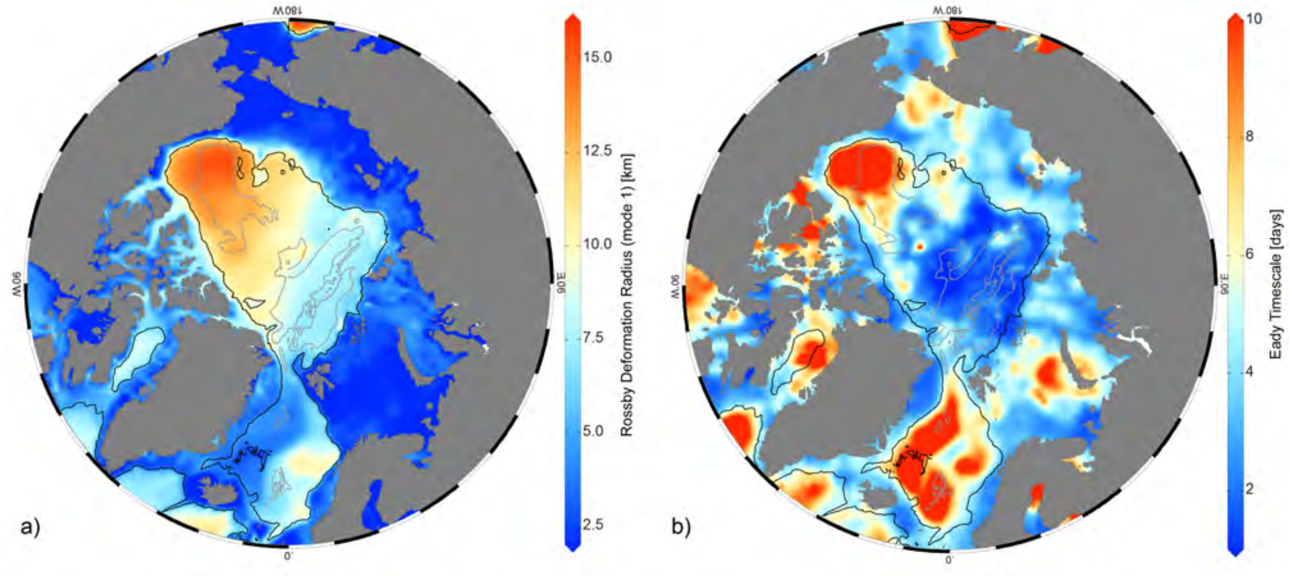

Figure 4. a) First baroclinic Rossby radius of deformation (km, computed from hydrographic climatology: WOD18, 2005-2017) following the method outlined by Chelton et al. (1998). b) An approximate Eady timescale ω^{-1} (days) calculated from (1) (see Smith, 2007) using the thermal wind shear estimated from the WOD18 climatology.

Armitage, T. W. K., Bacon, S., Ridout, A. L., Thomas, S. F., Aksenov, Y., & Wingham, D. J. (2016). Arctic sea surface height variability and change from satellite radar altimetry and GRACE, 2003-2014. *Journal of Geophysical Research: Oceans*, *121*(6), 4303–4322. doi: 10.1002/2015JC011579

Årthun, M., Eldevik, T., Smedsrud, L., Skagseth, Ø., & Ingvaldsen, R. (2012). Quantifying the influence of Atlantic heat on Barents Sea ice variability and retreat. *Journal of Climate*, *25*(13), 4736–4743.

Årthun, M., Eldevik, T., & Smedsrud, L. H. (2019). The role of Atlantic heat transport in future Arctic winter sea ice loss. *Journal of Climate*, *32*(11), 3327–3341.

Bebieva, Y., & Timmermans, M.-L. (2017). The relationship between double-diffusive intrusions and staircases in the Arctic Ocean. *Journal of Physical Oceanography*, *47*(4), 867–878.

Bebieva, Y., & Timmermans, M.-L. (2019). Double-diffusive layering in the Canada Basin: An explanation of along-layer temperature and salinity gradients. *Journal of Geophysical Research: Oceans*, *124*(1), 723–735.

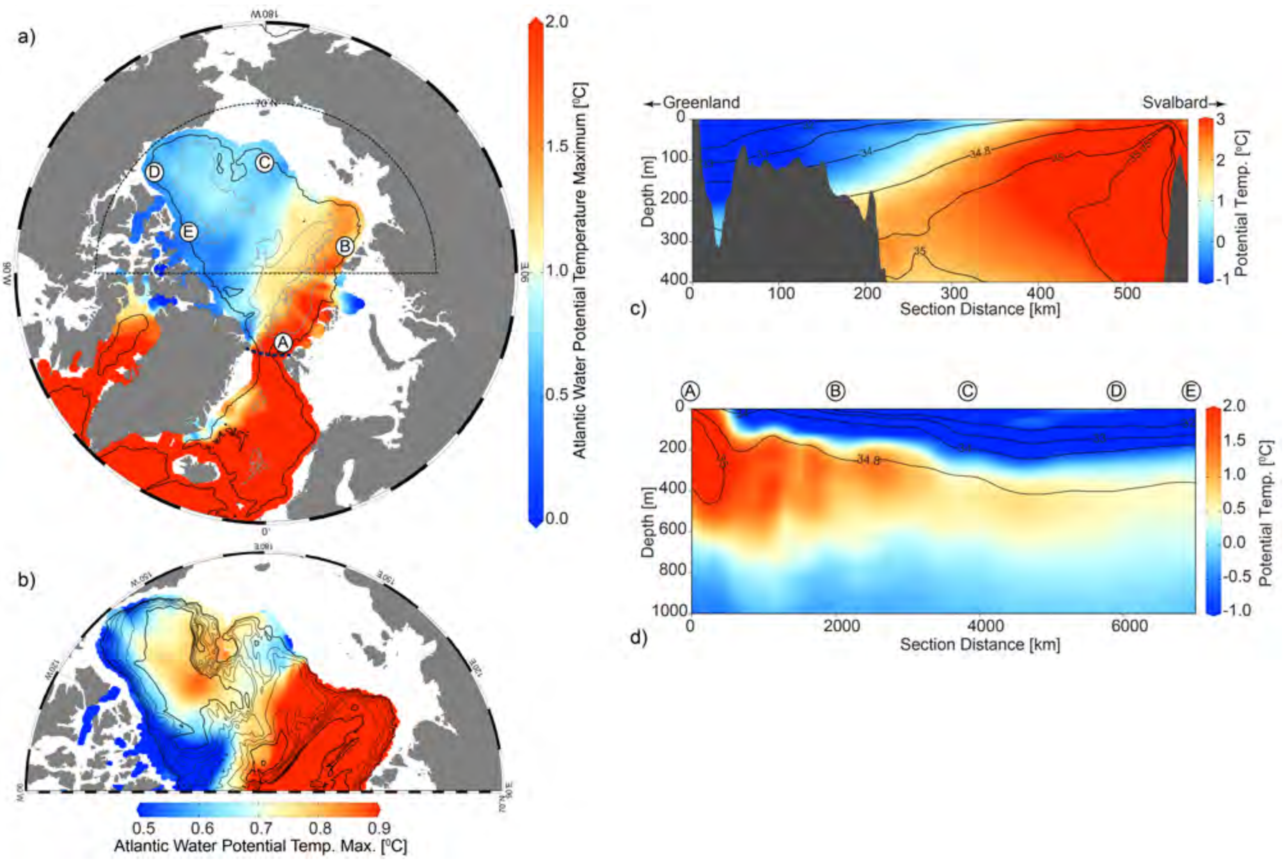

Figure 5. Maps of Atlantic Water potential temperature maximum (°C) for a) the Arctic Ocean and b) the sector bounded by the thin dotted black lines in a). Bathymetric contours in b) are in intervals of 500 m; the deepest contour shown is 3500 m. Sections of potential temperature (°C, colors) and salinity (contours) c) across Fram Strait from west to east along 80°N (thick dotted line shown in panel a; cooler, fresher water in the west flows south, while the warmer, saltier water to the east flows north, entering the Arctic Ocean from the Nordic Seas) and d) along the 1000 m isobath moving cyclonically around the Arctic Basin with letters A-E corresponding to their locations marked in panel a.

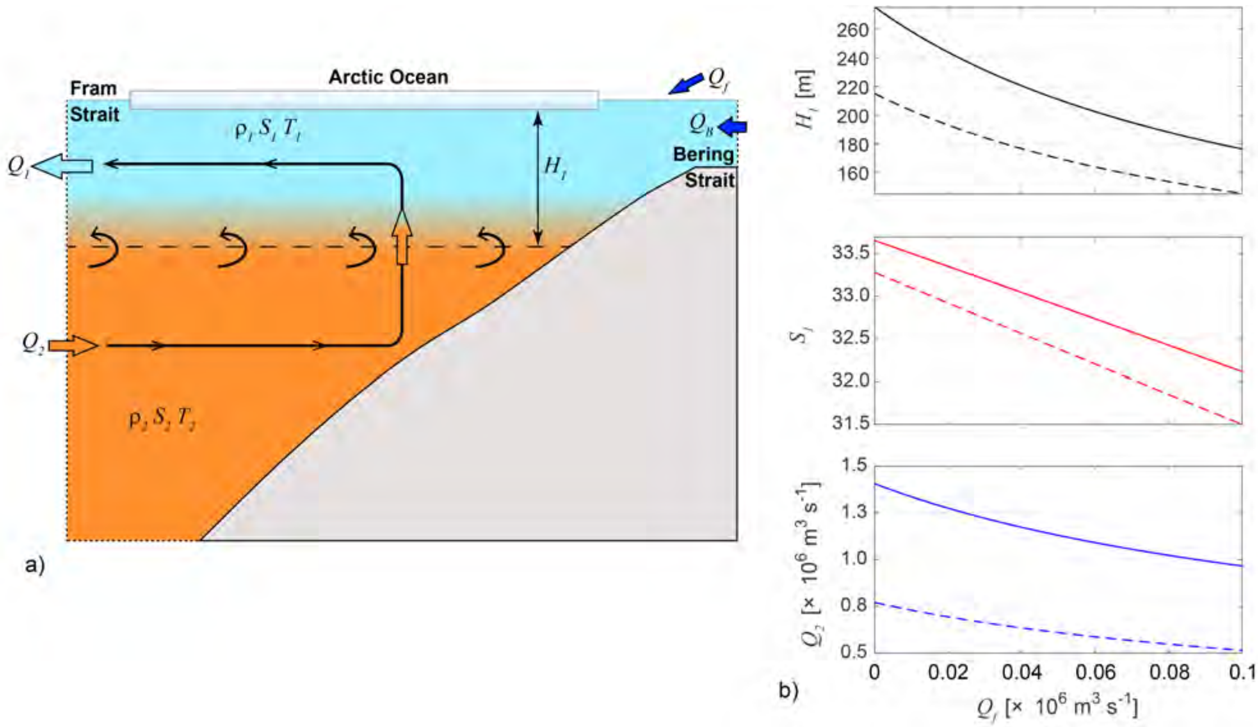

Figure 6. a) Schematic of an idealized 2-layer estuary (see Stigebrandt, 1981, his Figure 2). The upper layer constitutes Polar Water that flows from the Arctic Ocean to the Nordic Seas on the left side of the diagram, while the lower layer is renewed by Atlantic Water inflowing from the Nordic Seas to the Arctic Ocean. Mixing and entrainment of Atlantic Water into the upper layer drives the Atlantic Water inflow. b) Solutions to the system of equations (2)-(6): Upper layer thickness H_1 (top), upper layer salinity S_1 (middle) and Atlantic Water volume influx Q_2 (bottom) as functions of net freshwater input Q_f. Parameter values chosen for the calculations are given in the text, and solutions are shown for two different values of the mixing rate: u_*=0.55 cm s^{-1} (solid lines) and u_*=0.45 cm s^{-1} (dashed lines). For a fixed value of Q_f, larger mixing gives rise to a thicker, saltier upper layer exiting the Arctic Ocean, and a larger Atlantic Water volume influx Q_2 (see Rudels, 1989; Stigebrandt, 1981).

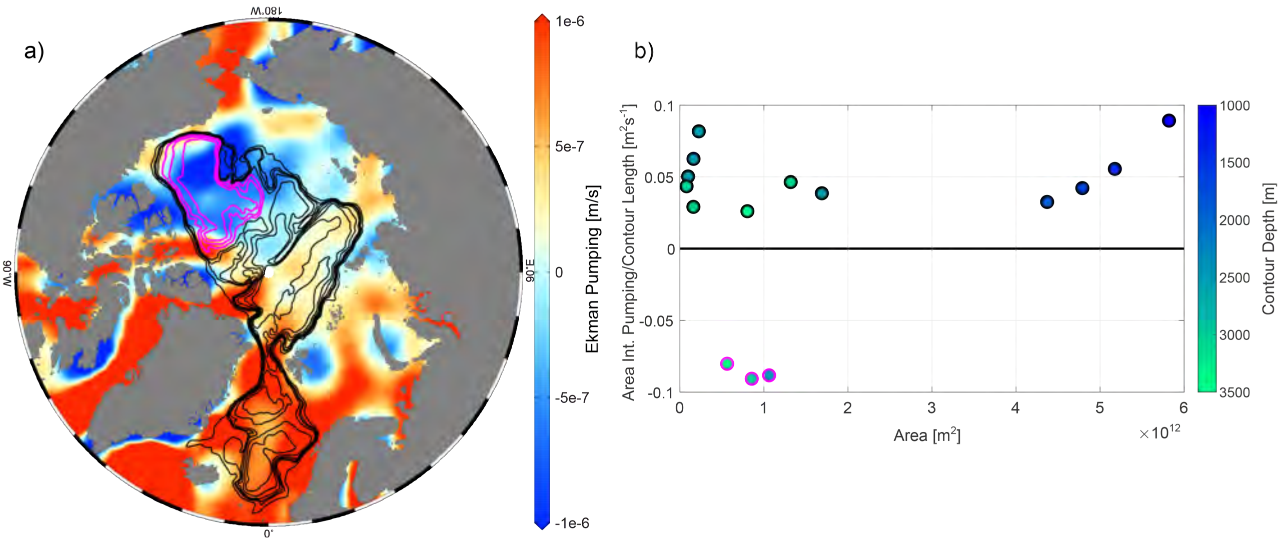

Figure 7. a) Annual average Ekman pumping (m/s, 2005-17) [color] and a selection of closed f/H contours; f/H contours effectively coincide with bathymetric contours at these latitudes. Black (magenta) contours enclose an area for which the area-integral of wind-stress curl is positive (negative). b) Area-integrated Ekman pumping per contour length (m^{2}s^{-1}) vs. area enclosed by the contour (m^2) for the contours shown in panel a (markers correspondingly outlined by black and magenta). Marker colors indicate the depth of the contours. See Nøst and Isachsen (2003), their figures 13 and 14.

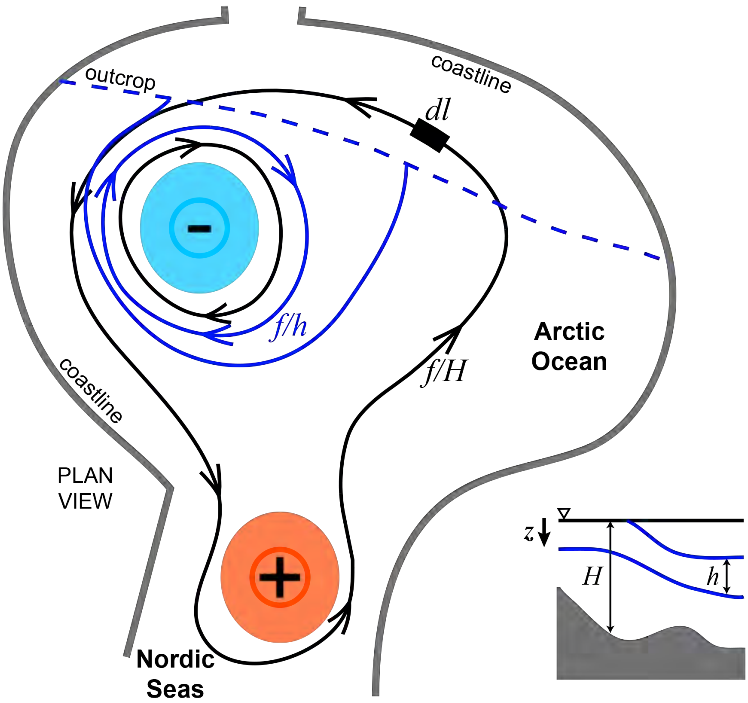

Figure 8. Plan-view schematic showing the main features of a wind-driven model of the circulation. f/H contours are shown in black with the direction of circulation along the contour governed by the sign of the wind-stress curl integrated over the area enclosed by the contour. The blue patch depicts the dominance of anticyclonic wind-stress curl in the Arctic Ocean (specifically the Beaufort Gyre region), and the red patch depicts the cyclonic wind-stress curl that dominates in the Nordic Seas. Blue contours indicate lines of constant potential vorticity for a layer bounded by two isopycnals (the section view shown in the inset shows isopycnals in blue).

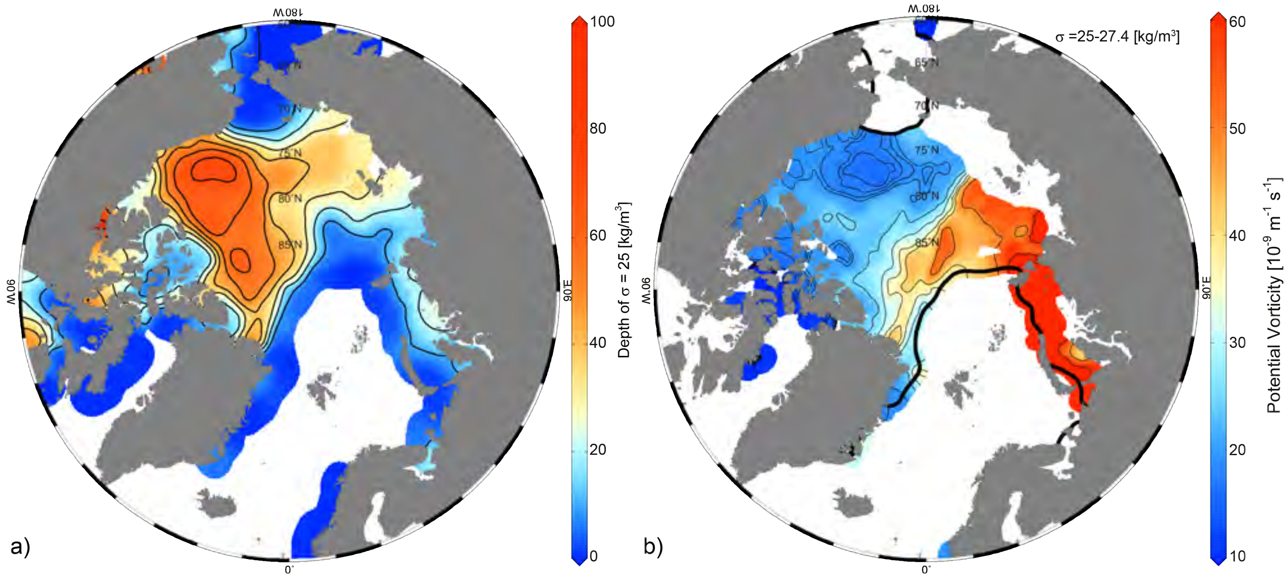

Figure 9. a) Depth of the σ=25 kg m^{-3} isopycnal. b) Potential vorticity (m^{-1}s^{-1}) of the σ=25 – 27.4 kg m^{-3} layer estimated by $f\delta\sigma/(h\rho_0)$, where $\delta\sigma$ is the density difference between the two density surfaces separated by a vertical distance h. The thick black contours indicate the σ=25 kg m^{-3} outcrop.

Belkin, I. M., & Levitus, S. (1996). Temporal variability of the subarctic front near the Charlie-Gibbs Fracture Zone. *Journal of Geophysical Research: Oceans*, *101*(C12), 28317–28324.

Belkin, I. M., Levitus, S., Antonov, J., & Malmberg, S.-A. (1998). "great salinity anomalies in the North Atlantic. *Progress in Oceanography*, *41*(1), 1–68.

Beszczynska-Möller, A., Fahrbach, E., Schauer, U., & Hansen, E. (2012). Variability in Atlantic water temperature and transport at the entrance to the Arctic Ocean, 1997–2010. *ICES Journal of Marine Science*, *69*(5), 852–863.

Boyd, T. J., Steele, M., Muench, R. D., & Gunn, J. T. (2002). Partial recovery of the Arctic Ocean halocline. *Geophysical Research Letters*, *29*(14), 2–1.

Boyer, T. P. (2018). World ocean database 2018. *NOAA Atlas NESDIS 87*.

Carmack, E., Aagaard, K., Swift, J., Perkin, R., McLaughlin, F., Macdonald, R., & Jones, E. (1998). Thermohaline transitions. *Coastal and Estuarine Studies*, 179–186.

Carmack, E., Polyakov, I., Padman, L., Fer, I., Hunke, E., Hutchings, J., . . . others (2015). Toward quantifying the increasing role of oceanic heat in sea ice loss

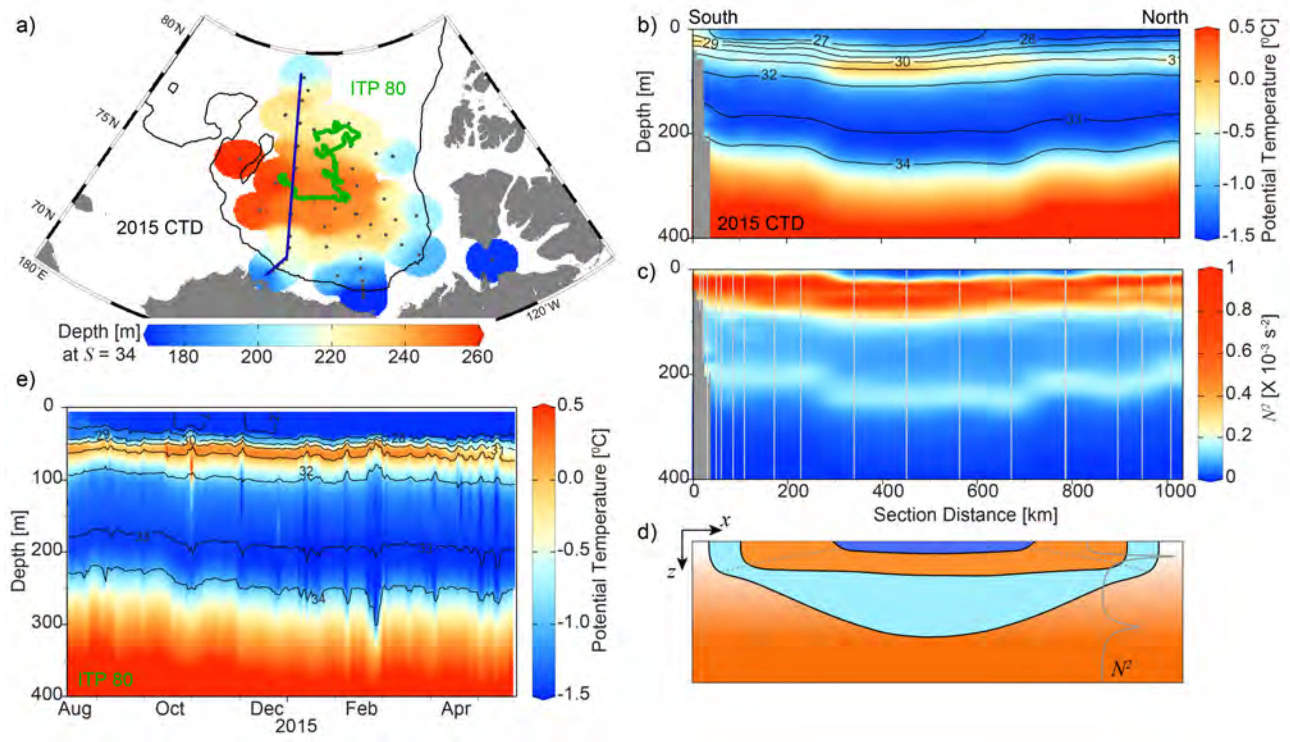

Figure 10. a) Depth of the S=34 isohaline from the 2015 Beaufort Gyre hydrographic expedition; CTD station locations are indicated by black dots. Sections from 2015 CTD data of b) potential temperature (°C, colors) and salinity (black contours) and c) buoyancy frequency (N^2, s^{-2}) from south (left) to north (right) along the blue line shown in panel a). d) Schematic cross section of the Beaufort Gyre where black lines represent isopycnals and colors represent temperature (blues, cold and oranges, warm); a layered configuration is shown to approximate the continuous stratification of the Beaufort Gyre, while the grey contour represents a typical stratification profile; grey dashed lines mark the base of the mixed layer. e) Depth-time section of potential temperature (°C, colors) and salinity (black contours) from an Ice-Tethered Profiler (ITP) that sampled in the Canada Basin in 2014-2015 along the green drift track shown in a), where the ITP drifted from north (August 2014) to south (May 2015).

in the new Arctic. *Bulletin of the American Meteorological Society*, *96*(12), 2079–2105.

Carmack, E. C. (2000). The Arctic Oceans freshwater budget: Sources, storage and export. In *The freshwater budget of the Arctic Ocean* (pp. 91–126). Springer.

Carmack, E. C. (2007). The alpha/beta ocean distinction: A perspective on freshwater fluxes, convection, nutrients and productivity in high-latitude seas. *Deep Sea Research Part II: Topical Studies in Oceanography*, *54*(23), 2578–2598.

Carmack, E. C., Yamamoto-Kawai, M., Haine, T. W., Bacon, S., Bluhm, B. A., Lique, C., … others (2016). Freshwater and its role in the Arctic marine System: Sources, disposition, storage, export, and physical and biogeochemical consequences in the Arctic and global oceans. *Journal of Geophysical Research: Biogeosciences*, *121*(3), 675–717.

Carpenter, J. R., & Timmermans, M.-L. (2012). Deep mesoscale eddies in the Canada Basin, Arctic Ocean. *Geophysical Research Letters*, *39*(20), 1–6. Retrieved from `http://doi.wiley.com/10.1029/2012GL053025` doi: 10.1029/2012GL053025

Chelton, D. B., Deszoeke, R. A., Schlax, M. G., El Naggar, K., & Siwertz, N. (1998). Geographical variability of the first baroclinic Rossby radius of deformation. *Journal of Physical Oceanography*, *28*(3), 433–460.

Coachman, L., & Barnes, C. (1963). The movement of Atlantic water in the Arctic Ocean. *Arctic*, *16*(1), 8–16.

Coachman, L. K. (1969). Physical oceanography in the Arctic Ocean: 1968. *Arctic*, *22*(3), 214–224.

Cochran, J. R., Edwards, M. H., & Coakley, B. J. (2006). Morphology and structure of the Lomonosov Ridge, Arctic Ocean. *Geochemistry, Geophysics, Geosystems*, *7*(5).

Collins, M., Knutti, R., Arblaster, J., Dufresne, J.-L., Fichefet, T., Friedlingstein, P., … Wehner, M. (2013). Long-term climate change: Projections, commitments and irreversibility [Book Section]. In T. Stocker et al. (Eds.), *Climate change 2013: The physical science basis. contribution of working group i to the fifth assessment report of the intergovernmental panel on climate change* (p. 10291136). Cambridge, United Kingdom and New York, NY, USA: Cambridge University Press. Retrieved from `www.climatechange2013.org` doi:

10.1017/CBO9781107415324.024

Comiso, J. C. (2012). Large decadal decline of the Arctic multiyear ice cover. *Journal of Climate*, *25*(4), 1176–1193.

D'Asaro, E. A., & Morison, J. H. (1992). Internal waves and mixing in the Arctic Ocean. *Deep Sea Research Part A. Oceanographic Research Papers*, *39*(2), S459–S484.

Delworth, T. L., Zeng, F., Vecchi, G. A., Yang, X., Zhang, L., & Zhang, R. (2016). The North Atlantic Oscillation as a driver of rapid climate change in the Northern Hemisphere. *Nature Geoscience*, *9*(7), 509.

de Steur, L., Hansen, E., Mauritzen, C., Beszczynska-Möller, A., & Fahrbach, E. (2014). Impact of recirculation on the East Greenland Current in Fram Strait: Results from moored current meter measurements between 1997 and 2009. *Deep Sea Research Part I: Oceanographic Research Papers*, *92*, 26–40.

Dewar, W. K. (1998). Topography and barotropic transport control by bottom friction. *Journal of marine research*, *56*(2), 295–328.

Dewey, S., Morison, J., Kwok, R., Dickinson, S., Morison, D., & Andersen, R. (2018, 2). Arctic Ice-Ocean Coupling and Gyre Equilibration Observed With Remote Sensing. *Geophysical Research Letters*. Retrieved from `http://doi.wiley.com/10.1002/2017GL076229` doi: 10.1002/2017GL076229

Dmitrenko, I. A., Kirillov, S. A., Forest, A., Gratton, Y., Volkov, D. L., Williams, W. J., ... Barber, D. G. (2016). Shelfbreak current over the canadian Beaufort Sea continental slope: Wind-driven events in January 2005. *Journal of Geophysical Research: Oceans*, *121*(4), 2447–2468.

Dosser, H. V., & Rainville, L. (2016). Dynamics of the changing near-inertial internal wave field in the Arctic Ocean. *Journal of Physical Oceanography*, *46*(2), 395–415.

Dosser, H. V., Rainville, L., & Toole, J. M. (2014). Near-inertial internal wave field in the Canada Basin from ice-tethered profilers. *Journal of Physical Oceanography*, *44*(2), 413–426.

Dosser, H. V., & Timmermans, M.-L. (2018). Inferring circulation and lateral eddy fluxes in the Arctic Oceans deep Canada Basin using an inverse method. *Journal of Physical Oceanography*, *48*(2), 245–260.

Ekman, V. W., et al. (1905). On the influence of the Earth's rotation on ocean-currents. *Almqvist & Wiksells boktryckeri, A.-B.,*.

Eldevik, T., & Nilsen, J. E. Ø. (2013). The Arctic–Atlantic thermohaline circulation. *Journal of Climate*, *26*(21), 8698–8705.

Fer, I. (2009). Weak vertical diffusion allows maintenance of cold halocline in the central Arctic. *Atmospheric and Oceanic Science Letters*, *2*(3), 148–152.

Fetterer, F., Knowles, K., Meier, W., Savoie, M., & Windnagel, A. (2017). Updated daily Sea Ice Index version 3 Boulder Colorado USA. *NSIDC: National Snow and Ice Data Center*. doi: 10.7265/N5K072F8

Garcia, H., Boyer, T., Baranova, O., Locarnini, R., Mishonov, A., Grodsky, A., ... Zweng, M. (2019). World Ocean Atlas 2018: Product documentation. *Ocean Climate Laboratory NCEI, NESDIS, NOAA*.

Garrett, C., & Horne, E. (1978). Frontal circulation due to cabbeling and double diffusion. *Journal of Geophysical Research: Oceans*, *83*(C9), 4651–4656.

Gent, P. R., & Mcwilliams, J. C. (1990). Isopycnal mixing in ocean circulation models. *Journal of Physical Oceanography*, *20*(1), 150–155.

Gray, A. R., & Riser, S. C. (2014). A global analysis of Sverdrup balance using absolute geostrophic velocities from Argo. *Journal of Physical Oceanography*, *44*(4), 1213–1229.

Guthrie, J. D., Fer, I., & Morison, J. (2015). Observational validation of the diffusive convection flux laws in the Amundsen Basin, Arctic Ocean. *Journal of Geophysical Research: Oceans*, *120*(12), 7880–7896.

Haine, T. W., & Martin, T. (2017). The Arctic-Subarctic sea ice system is entering a seasonal regime: Implications for future Arctic amplification. *Scientific reports*, *7*(1), 4618.

Haine, T. W. N., Curry, B., Gerdes, R., Hansen, E., Karcher, M., Lee, C., ... Woodgate, R. (2015). Arctic freshwater export: Status, mechanisms, and prospects. *Global and Planetary Change*, *125*, 13–35. Retrieved from `http://dx.doi.org/10.1016/j.gloplacha.2014.11.013` doi: 10.1016/j.gloplacha.2014.11.013

Halle, C., & Pinkel, R. (2003). Internal wave variability in the Beaufort Sea during the winter of 1993/1994. *Journal of Geophysical Research: Oceans*, *108*(C7).

Hansen, B., Østerhus, S., Turrell, W. R., Jónsson, S., Valdimarsson, H., Hátún, H., & Olsen, S. M. (2008). The inflow of Atlantic water, heat, and salt to the

Nordic seas across the Greenland–Scotland ridge. In *Arctic–Subarctic ocean fluxes* (pp. 15–43). Springer.

Holloway, G. (1992). Representing topographic stress for large-scale ocean models. *Journal of Physical Oceanography*, *22*(9), 1033–1046.

Holloway, G. (2004). From classical to statistical ocean dynamics. *Surveys in Geophysics*, *25*(3-4), 203–219.

Holloway, G., & Proshutinsky, A. (2007). Role of tides in Arctic ocean/ice climate. *Journal of Geophysical Research: Oceans*, *112*(C4).

Holmes, R. M., McClelland, J. W., Peterson, B. J., Tank, S. E., Bulygina, E., Eglinton, T. I., … others (2012). Seasonal and annual fluxes of nutrients and organic matter from large rivers to the Arctic Ocean and surrounding seas. *Estuaries and Coasts*, *35*(2), 369–382.

Ingvaldsen, R., Loeng, H., & Asplin, L. (2002). Variability in the Atlantic inflow to the barents Sea based on a one-year time series from moored current meters. *Continental Shelf Research*, *22*(3), 505–519.

Isachsen, P., LaCasce, J., Mauritzen, C., & Häkkinen, S. (2003). Wind-driven variability of the large-scale recirculating flow in the Nordic Seas and Arctic Ocean. *Journal of Physical Oceanography*, *33*(12), 2534–2550.

Iselin, C. (1939). The influence of vertical and lateral turbulence on the characteristics of the waters at mid-depths. *Eos Trans. Am. Geophys. Union*, *20*, 414–417.

Ivanov, V., Alexeev, V., Koldunov, N. V., Repina, I., Sandø, A. B., Smedsrud, L. H., & Smirnov, A. (2016). Arctic Ocean heat impact on regional ice decay: A suggested positive feedback. *Journal of Physical Oceanography*, *46*(5), 1437–1456.

Jakobsson, M., Macnab, R., Mayer, L., Anderson, R., Edwards, M., Hatzky, J., … Johnson, P. (2008). An improved bathymetric portrayal of the Arctic Ocean: Implications for ocean modeling and geological, geophysical and oceanographic analyses. *Geophysical Research Letters*, *35*(7).

Jakobsson, M., Mayer, L., Coakley, B., Dowdeswell, J. A., Forbes, S., Fridman, B., … others (2012). The international bathymetric chart of the Arctic Ocean (ibcao) version 3.0. *Geophysical Research Letters*, *39*(12).

Kalnay, E., Kanamitsu, M., Kistler, R., Collins, W., Deaven, D., Gandin, L., … others (1996). The NCEP/NCAR 40-year reanalysis project. *Bulletin of the*

American meteorological Society, *77*(3), 437–472.

Karcher, M., Kauker, F., Gerdes, R., Hunke, E., & Zhang, J. (2007). On the dynamics of Atlantic water circulation in the Arctic Ocean. *Journal of Geophysical Research: Oceans*, *112*(C4).

Kowalik, Z., & Proshutinsky, A. Y. (1993). Diurnal tides in the Arctic Ocean. *Journal of Geophysical Research: Oceans*, *98*(C9), 16449–16468.

Kowalik, Z., & Proshutinsky, A. Y. (1995). Topographic enhancement of tidal motion in the western Barents Sea. *Journal of Geophysical Research: Oceans*, *100*(C2), 2613–2637.

Kozlov, I., Artamonova, A., Manucharyan, G., & Kubryakov, A. (2019). Eddies in the western Arctic Ocean from spaceborne SAR observations over open ocean and marginal ice zones. *Journal of Geophysical Research: Oceans*.

Krishfield, R., Toole, J., Proshutinsky, A., & Timmermans, M.-L. (2008). Automated ice-tethered profilers for seawater observations under pack ice in all seasons. *Journal of Atmospheric and Oceanic Technology*, *25*(11), 2091–2105. doi: 10.1175/2008JTECHO587.1

Krishfield, R. A., & Perovich, D. K. (2005). Spatial and temporal variability of oceanic heat flux to the Arctic ice pack. *Journal of Geophysical Research: Oceans*, *110*(C7).

Krishfield, R. A., Proshutinsky, A., Tateyama, K., Williams, W. J., Carmack, E. C., McLaughlin, F. A., & Timmermans, M.-L. (2014). Deterioration of perennial sea ice in the Beaufort Gyre from 2003 to 2012 and its impact on the oceanic freshwater cycle. *Journal of Geophysical Research: Oceans*, *119*(2), 1271–1305. doi: 10.1002/2013JC008999

Kwok, R. (2009). Outflow of Arctic Ocean sea ice into the Greenland and Barents Seas: 1979–2007. *Journal of Climate*, *22*(9), 2438–2457.

Kwok, R. (2018). Arctic sea ice thickness, volume, and multiyear ice coverage: losses and coupled variability (1958–2018). *Environmental Research Letters*, *13*(10), 105005.

Kwok, R., Spreen, G., & Pang, S. (2013). Arctic sea ice circulation and drift speed: Decadal trends and ocean currents. *Journal of Geophysical Research: Oceans*, *118*(5), 2408–2425.

Lambert, E., Eldevik, T., & Haugan, P. M. (2016). How northern freshwater input can stabilise thermohaline circulation. *Tellus A: Dynamic Meteorology and Oceanography*, *68*(1), 31051.

LeBlond, P. H. (1980). On the surface circulation in some channels of the Canadian Arctic archipelago. *Arctic*, 189–197.

Ledwell, J., Montgomery, E., Polzin, K., Laurent, L. S., Schmitt, R., & Toole, J. (2000). Evidence for enhanced mixing over rough topography in the abyssal ocean. *Nature*, *403*(6766), 179.

Lenn, Y.-D., Wiles, P., Torres-Valdes, S., Abrahamsen, E., Rippeth, T., Simpson, J., … others (2009). Vertical mixing at intermediate depths in the Arctic boundary current. *Geophysical Research Letters*, *36*(5).

Lincoln, B. J., Rippeth, T. P., Lenn, Y.-D., Timmermans, M. L., Williams, W. J., & Bacon, S. (2016). Wind-driven mixing at intermediate depths in an ice-free Arctic Ocean. *Geophysical Research Letters*, *43*(18), 9749–9756.

Lind, S., Ingvaldsen, R. B., & Furevik, T. (2018). Arctic warming hotspot in the northern Barents Sea linked to declining sea-ice import. *Nature climate change*, *8*(7), 634.

Luneva, M. V., Aksenov, Y., Harle, J. D., & Holt, J. T. (2015). The effects of tides on the water mass mixing and sea ice in the Arctic Ocean. *Journal of Geophysical Research: Oceans*, *120*(10), 6669–6699.

Luyten, J., Pedlosky, J., & Stommel, H. (1983). The ventilated thermocline. *J. Phys. Oceanogr.*, *13*, 292–309.

Manley, T. O., & Hunkins, K. (1985). Mesoscale Eddies of the Arctic Ocean. *Journal of Geophysical Research C Oceans*, *90*(C3), 19. Retrieved from `http://onlinelibrary.wiley.com/doi/10.1029/JC090iC03p04911/abstract` doi: 10.1029/JC090iC03p04911

Manucharyan, G., & Isachsen, P. (2019). Critical role of continental slopes in halocline and eddy dynamics of the ekman-driven Beaufort Gyre. *Journal of Geophysical Research: Oceans*, *124*(4), 2679–2696.

Manucharyan, G. E., Spall, M. A., & Thompson, A. F. (2016). A Theory of the Wind-Driven Beaufort Gyre Variability. *Journal of Physical Oceanography*(2013), 3263–3278. doi: 10.1175/JPO-D-16-0091.1

Manucharyan, G. E., Thompson, A. F., & Spall, M. A. (2017). Eddy Memory Mode of Multidecadal Variability in Residual-Mean Ocean Circulations with

Application to the Beaufort Gyre. *Journal of Physical Oceanography*, *47*(4), 855–866. Retrieved from `http://journals.ametsoc.org/doi/10.1175/JPO-D-16-0194.1` doi: 10.1175/JPO-D-16-0194.1

Marshall, J., Jamous, D., & Nilsson, J. (2001). Entry, flux, and exit of potential vorticity in ocean circulation. *Journal of physical oceanography*, *31*(3), 777–789.

Marshall, J., & Radko, T. (2003). Residual-mean solutions for the Antarctic Circumpolar Current and its associated overturning circulation. *Journal of Physical Oceanography*, *33*(11), 2341–2354.

Marshall, J., & Speer, K. (2012). Closure of the meridional overturning circulation through Southern Ocean upwelling. *Nature Geoscience*, *5*(3), 171.

Mauldin, A., Schlosser, P., Newton, R., Smethie Jr, W., Bayer, R., Rhein, M., & Jones, E. P. (2010). The velocity and mixing time scale of the Arctic Ocean Boundary Current estimated with transient tracers. *Journal of Geophysical Research: Oceans*, *115*(C8).

Mauritzen, C. (1996). Production of dense overflow waters feeding the North Atlantic across the Greenland-Scotland ridge. part 2: An inverse model. *Deep Sea Research Part I: Oceanographic Research Papers*, *43*(6), 807–835.

Maykut, G., & McPhee, M. G. (1995). Solar heating of the Arctic mixed layer. *Journal of Geophysical Research: Oceans*, *100*(C12), 24691–24703.

Maykut, G. A., & Untersteiner, N. (1971). Some results from a time-dependent thermodynamic model of sea ice. *Journal of Geophysical Research*, *76*(6), 1550–1575.

McClelland, J. W., Holmes, R., Dunton, K., & Macdonald, R. (2012). The Arctic Ocean estuary. *Estuaries and Coasts*, *35*(2), 353–368.

McLaughlin, F., Carmack, E., Macdonald, R., & Bishop, J. (1996). Physical and geochemical properties across the Atlantic/Pacific water mass front in the southern Canadian Basin. *Journal of Geophysical Research: Oceans*, *101*(C1), 1183–1197.

McLaughlin, F., Carmack, E., Macdonald, R., Melling, H., Swift, J., Wheeler, P., ... Sherr, E. (2004). The joint roles of Pacific and Atlantic-origin waters in the Canada Basin, 1997–1998. *Deep Sea Research Part I: Oceanographic Research Papers*, *51*(1), 107–128.

McLaughlin, F. A., Carmack, E. C., Williams, W. J., Zimmermann, S., Shimada, K., & Itoh, M. (2009). Joint effects of boundary currents and thermohaline intrusions on the warming of Atlantic water in the Canada Basin, 1993–2007. *Journal of Geophysical Research: Oceans*, *114*(C1).

McPhee, M. G. (2013). Intensification of geostrophic currents in the Canada Basin, Arctic Ocean. *Journal of Climate*, *26*(10), 3130–3138. doi: 10.1175/JCLI-D-12-00289.1

Meneghello, G., Marshall, J., Campin, J.-M., Doddridge, E., & Timmermans, M.-L. (2018). The ice-ocean governor: Ice-ocean stress feedback limits Beaufort Gyre spin-up. *Geophysical Research Letters*, *45*(20), 11–293.

Meneghello, G., Marshall, J., Cole, S. T., & Timmermans, M.-L. (2017, 11). Observational inferences of lateral eddy diffusivity in the halocline of the Beaufort Gyre. *Geophysical Research Letters*, *44*. Retrieved from `http://doi.wiley.com/10.1002/2017GL075126` doi: 10.1002/2017GL075126

Meneghello, G., Marshall, J., Timmermans, M.-L., & Scott, J. (2018). Observations of seasonal upwelling and downwelling in the Beaufort Sea mediated by sea ice. *J. Phys. Oceanogr.*, *in press*. doi: 10.1175/JPO-D-17-0188.1

Mensa, J., Timmermans, M.-L., Kozlov, I., Williams, W., & Özgökmen, T. (2018). Surface drifter observations from the Arctic Ocean's Beaufort Sea: Evidence for submesoscale dynamics. *Journal of Geophysical Research: Oceans*, *123*(4), 2635–2645.

Moore, G., Schweiger, A., Zhang, J., & Steele, M. (2018). Collapse of the 2017 winter Beaufort High: A response to thinning sea ice? *Geophysical Research Letters*, *45*(6), 2860–2869.

Morison, J., Kwok, R., Peralta-Ferriz, C., Alkire, M., Rigor, I., Andersen, R., & Steele, M. (2012). Changing Arctic Ocean freshwater pathways. *Nature*, *481*(7379), 66.

Morison, J., Long, C., & Levine, M. (1985). The dissipation of internal wave energy under Arctic ice. *J. Geophys. Res*, *90*, 11–959.

Morison, J., Steele, M., & Andersen, R. (1998). Hydrography of the upper Arctic Ocean measured from the nuclear submarine USS pargo. *Deep Sea Research Part I: Oceanographic Research Papers*, *45*(1), 15–38.

Morison, J., Steele, M., Kikuchi, T., Falkner, K., & Smethie, W. (2006). Relaxation of central Arctic Ocean hydrography to pre-1990s climatology. *Geophysical Re-*

search Letters, *33*(17).

Moros, M., Jansen, E., Oppo, D. W., Giraudeau, J., & Kuijpers, A. (2012). Reconstruction of the late-holocene changes in the sub-Arctic front position at the Reykjanes Ridge, North Atlantic. *The Holocene*, *22*(8), 877–886.

Muilwijk, M., Smedsrud, L. H., Ilicak, M., & Drange, H. (2018). Atlantic water heat transport variability in the 20th century Arctic Ocean from a global ocean model and observations. *Journal of Geophysical Research: Oceans*, *123*(11), 8159–8179.

Münchow, A., Melling, H., & Falkner, K. K. (2006). An observational estimate of volume and freshwater flux leaving the Arctic Ocean through Nares Strait. *Journal of Physical Oceanography*, *36*(11), 2025–2041.

Munk, W. H. (1950). On the wind-driven ocean circulation. *Journal of meteorology*, *7*(2), 80–93.

Nansen, F. (1897). Some results of the Norwegian Arctic expedition, 1893–96. *Scottish Geographical Magazine*, *13*(5), 225–246.

Nansen, F. (1902). The oceanography of the North Polar Basin. the Norwegian North Polar Expedition 1893-1896. *Scient. Results*, *3*(9).

Nazarenko, L., Holloway, G., & Tausnev, N. (1998). Dynamics of transport of Atlantic signature in the Arctic Ocean. *Journal of Geophysical Research: Oceans*, *103*(C13), 31003–31015.

Nikolopoulos, A., Pickart, R. S., Fratantoni, P. S., Shimada, K., Torres, D. J., & Jones, E. P. (2009). The western Arctic boundary current at 152 w: Structure, variability, and transport. *Deep Sea Research Part II: Topical Studies in Oceanography*, *56*(17), 1164–1181.

Nøst, O. A., & Isachsen, P. E. (2003). The large-scale time-mean ocean circulation in the Nordic Seas and Arctic Ocean estimated from simplified dynamics. *Journal of Marine Research*, *61*(2), 175–210.

Nurser, A. J. G., & Bacon, S. (2014). The Rossby radius in the Arctic Ocean. *Ocean Science*, *10*(6), 967–975. doi: 10.5194/os-10-967-2014

Oldenburg, D., Armour, K. C., Thompson, L., & Bitz, C. M. (2018). Distinct mechanisms of ocean heat transport into the Arctic under internal variability and climate change. *Geophysical Research Letters*, *45*(15), 7692–7700.

Orvik, K. A., & Niiler, P. (2002). Major pathways of atlantic water in the northern

North Atlantic and Nordic Seas toward Arctic. *Geophysical Research Letters*, *29*(19), 2–1.

Overland, J., Hanna, E., Hanssen-Bauer, I., Kim, S.-J., Walsh, J., Wang, M., & Bhatt, U. (2019). [the Arctic] surface air temperature [in "State of the Climate in 2018"]. *Bull. Amer. Meteor. Soc.*, *100*(9), S142–S144. doi: 10.1175/2019BAMSStateoftheClimate.1

Padman, L. (1995). Small-scale physical processes in the Arctic Ocean. *COASTAL AND ESTUARINE STUDIES*, 97–97.

Padman, L., & Dillon, T. M. (1987). Vertical heat fluxes through the Beaufort Sea thermohaline staircase. *Journal of Geophysical Research: Oceans*, *92*(C10), 10799–10806.

Padman, L., & Dillon, T. M. (1989). Thermal microstructure and internal waves in the Canada Basin diffusive staircase. *Deep Sea Research Part A. Oceanographic Research Papers*, *36*(4), 531–542.

Padman, L., Plueddemann, A. J., Muench, R. D., & Pinkel, R. (1992). Diurnal tides near the Yermak Plateau. *Journal of Geophysical Research: Oceans*, *97*(C8), 12639–12652.

Peralta-Ferriz, C., & Woodgate, R. A. (2015). Seasonal and interannual variability of pan-arctic surface mixed layer properties from 1979 to 2012 from hydrographic data, and the dominance of stratification for multiyear mixed layer depth shoaling. *Progress in Oceanography*, *134*, 19–53.

Perner, K., Moros, M., Jansen, E., Kuijpers, A., Troelstra, S. R., & Prins, M. A. (2018). Subarctic front migration at the Reykjanes Ridge during the mid-to late holocene: evidence from planktic foraminifera. *Boreas*, *47*(1), 175–188.

Perovich, D., Meier, W., Tschudi, M., Farrell, S., Hendricks, S., Gerland, S., … Webster, M. (2019). [the Arctic] sea ice cover [in "State of the Climate in 2018"]. *Bull. Amer. Meteor. Soc.*, *100*(9), S146–S150. doi: 10.1175/2019BAMSStateoftheClimate.1

Perovich, D. K., & Richter-Menge, J. A. (2009). Loss of sea ice in the Arctic. *Annual review of marine science*, *1*, 417–441.

Perovich, D. K., Richter-Menge, J. A., Jones, K. F., & Light, B. (2008). Sunlight, water, and ice: Extreme Arctic sea ice melt during the summer of 2007. *Geophysical Research Letters*, *35*(11).

Perovich, D. K., Richter-Menge, J. A., Jones, K. F., Light, B., Elder, B. C., Polashenski, C., … Lindsay, R. (2011). Arctic sea-ice melt in 2008 and the role of solar heating. *Annals of Glaciology*, *52*(57), 355–359.

Peterson, A. K., Fer, I., McPhee, M. G., & Randelhoff, A. (2017). Turbulent heat and momentum fluxes in the upper ocean under Arctic sea ice. *Journal of Geophysical Research: Oceans*, *122*(2), 1439–1456.

Pickart, R. S. (2004). Shelfbreak circulation in the Alaskan Beaufort Sea: Mean structure and variability. *Journal of Geophysical Research: Oceans*, *109*(C4).

Pickart, R. S., Weingartner, T. J., Pratt, L. J., Zimmermann, S., & Torres, D. J. (2005). Flow of winter-transformed Pacific water into the Western Arctic. *Deep Sea Research Part II: Topical Studies in Oceanography*, *52*(24-26), 3175–3198.

Pinkel, R. (2005). Near-inertial wave propagation in the western Arctic. *Journal of physical oceanography*, *35*(5), 645–665.

Pistone, K., Eisenman, I., & Ramanathan, V. (2014). Observational determination of albedo decrease caused by vanishing Arctic sea ice. *Proceedings of the National Academy of Sciences*, *111*(9), 3322–3326.

Plueddemann, A., Krishfield, R., Takizawa, T., Hatakeyama, K., & Honjo, S. (1998). Upper ocean velocities in the Beaufort Gyre. *Geophysical research letters*, *25*(2), 183–186.

Pnyushkov, A., Polyakov, I. V., Padman, L., & Nguyen, A. T. (2018). Structure and dynamics of mesoscale eddies over the Laptev Sea continental slope in the Arctic Ocean. *Ocean Science*, *14*(5), 1329–1347.

Polyakov, I. (2001). An eddy parameterization based on maximum entropy production with application to modeling of the Arctic Ocean circulation. *Journal of physical oceanography*, *31*(8), 2255–2270.

Polyakov, I. V., Pnyushkov, A. V., Alkire, M. B., Ashik, I. M., Baumann, T. M., Carmack, E. C., … others (2017). Greater role for atlantic inflows on sea-ice loss in the Eurasian Basin of the Arctic Ocean. *Science*, *356*(6335), 285–291.

Polyakov, I. V., Pnyushkov, A. V., Rember, R., Ivanov, V. V., Lenn, Y.-D., Padman, L., & Carmack, E. C. (2012). Mooring-based observations of double-diffusive staircases over the Laptev Sea slope. *Journal of Physical Oceanography*, *42*(1), 95–109.

Polyakov, I. V., Timokhov, L. A., Alexeev, V. A., Bacon, S., Dmitrenko, I. A., Fortier, L., … others (2010). Arctic Ocean warming contributes to reduced polar ice cap. *Journal of Physical Oceanography*, *40*(12), 2743–2756.

Proshutinsky, A., Bourke, R., & McLaughlin, F. (2002). The role of the Beaufort Gyre in Arctic climate variability: Seasonal to decadal climate scales. *Geophysical Research Letters*, *29*(23), 15–1.

Proshutinsky, A., Dukhovskoy, D., Timmermans, M.-l., Krishfield, R., & Bamber, J. L. (2015). Arctic circulation regimes. *Philosophical transactions. Series A, Mathematical, physical, and engineering sciences*, *373*(2052), 20140160. Retrieved from `http://rsta.royalsocietypublishing.org/content/373/2052/20140160` doi: 10.1098/rsta.2014.0160

Proshutinsky, A., Krishfield, R., & Timmermans, M.-L. (2019). Preface to special issue forum for Arctic Ocean Modeling and Observational Synthesis (FAMOS) 2: Beaufort Gyre phenomenon. *Journal of Geophysical Research: Oceans*.

Proshutinsky, A., Krishfield, R., Timmermans, M.-l., Toole, J., Carmack, E., Mclaughlin, F., … Shimada, K. (2009). Beaufort Gyre freshwater reservoir : State and variability from observations. *Journal of Geophysical Research*, *114*, 1–25. doi: 10.1029/2008JC005104

Proshutinsky, A. e. a. (2019). Analysis of the Beaufort Gyre freshwater content in 2003-2018. *Journal of Geophysical Research*, *xxx*(xxx), xxx. doi: 1xxx

Proshutinsky, A. Y., & Johnson, M. A. (1997). Two circulation regimes of the wind-driven Arctic Ocean. *Journal of Geophysical Research: Oceans*, *102*(C6), 12493–12514. doi: 10.1029/97JC00738

Rabe, B., Karcher, M., Kauker, F., Schauer, U., Toole, J. M., Krishfield, R. A., … Su, J. (2014). Arctic Ocean basin liquid freshwater storage trend 1992–2012. *Geophysical Research Letters*, *41*(3), 961–968.

Rainville, L., Lee, C. M., & Woodgate, R. A. (2011). Impact of wind-driven mixing in the Arctic Ocean. *Oceanography*, *24*(3), 136–145.

Rainville, L., & Winsor, P. (2008). Mixing across the Arctic Ocean: Microstructure observations during the Beringia 2005 expedition. *Geophysical Research Letters*, *35*(8).

Rainville, L., & Woodgate, R. A. (2009). Observations of internal wave generation in the seasonally ice-free Arctic. *Geophysical Research Letters*, *36*(23).

Reynolds, R. W., Smith, T. M., Liu, C., Chelton, D. B., Casey, K. S., & Schlax, M. G. (2007). Daily high-resolution-blended analyses for sea surface temperature. *Journal of Climate*, *20*(22), 5473–5496.

Rhines, P. B. (1975). Waves and turbulence on a beta-plane. *Journal of Fluid Mechanics*, *69*(3), 417–443.

Richter-Menge, J., Jeffries, M., & Osborne, E. (2018). The Arctic [in "State of the Climate in 2017"]. *Bull. Amer. Meteor. Soc.*, *99*(8), S143S173. doi: 10.1175/2018BAMSStateoftheClimate.1

Rigor, I. G., Wallace, J. M., & Colony, R. L. (2002). Response of sea ice to the Arctic Oscillation. *Journal of Climate*, *15*(18), 2648–2663.

Rippeth, T. P., Lincoln, B. J., Lenn, Y.-D., Green, J. M., Sundfjord, A., & Bacon, S. (2015). Tide-mediated warming of Arctic halocline by Atlantic heat fluxes over rough topography. *Nature Geoscience*, *8*(3), 191.

Rippeth, T. P., Vlasenko, V., Stashchuk, N., Scannell, B. D., Green, J. M., Lincoln, B. J., & Bacon, S. (2017). Tidal conversion and mixing poleward of the critical latitude (an Arctic case study). *Geophysical Research Letters*, *44*(24), 12–349.

Roden, G. I. (1970). Aspects of the mid-Pacific transition zone. *Journal of Geophysical Research*, *75*(6), 1097–1109.

Roden, G. I. (1991). Subarctic-subtropical transition zone of the North Pacific: large-scale aspects and mesoscale structure. *NOAA Technical Report NMFS*, *105*, 1–38.

Rudels, B. (1989). The formation of polar surface water, the ice export and the exchanges through the Fram Strait. *Progress in Oceanography*, *22*(3), 205–248.

Rudels, B. (2015). Arctic Ocean circulation, processes and water masses: A description of observations and ideas with focus on the period prior to the International Polar Year 2007–2009. *Progress in Oceanography*, *132*, 22–67.

Rudels, B., Anderson, L., & Jones, E. (1996). Formation and evolution of the surface mixed layer and halocline of the Arctic Ocean. *Journal of Geophysical Research: Oceans*, *101*(C4), 8807–8821.

Rudels, B., Jones, E., Anderson, L., & Kattner, G. (1994). On the intermediate depth waters of the Arctic Ocean. *The polar oceans and their role in shaping the global environment*, *85*, 33–46.

Rudels, B., Kuzmina, N., Schauer, U., Stipa, T., & Zhurbas, V. (2009). Double-diffusive convection and interleaving in the Arctic Ocean–distribution and importance. *Geophysica*, *45*(1-2), 199–213.

Rudels, B., et al. (2012). Arctic Ocean circulation and variability-advection and external forcing encounter constraints and local processes. *Ocean Science*.

Schauer, U., & Beszczynska-Möller, A. (2009). Problems with estimating oceanic heat transport-conceptual remarks for the case of Fram Strait in the Arctic Ocean. *Ocean Science Discussions*, *6*, 1007–1029.

Schauer, U., Fahrbach, E., Osterhus, S., & Rohardt, G. (2004). Arctic warming through the Fram Strait: Oceanic heat transport from 3 years of measurements. *Journal of Geophysical Research: Oceans*, *109*(C6).

Schauer, U., Loeng, H., Rudels, B., Ozhigin, V. K., & Dieck, W. (2002). Atlantic water flow through the Barents and Kara Seas. *Deep Sea Research Part I: Oceanographic Research Papers*, *49*(12), 2281–2298.

Serreze, M. C., Barrett, A. P., Slater, A. G., Steele, M., Zhang, J., & Trenberth, K. E. (2007). The large-scale energy budget of the Arctic. *Journal of Geophysical Research: Atmospheres*, *112*(D11).

Serreze, M. C., Barrett, A. P., Slater, A. G., Woodgate, R. A., Aagaard, K., Lammers, R. B., ... Lee, C. M. (2006). The large-scale freshwater cycle of the Arctic. *Journal of Geophysical Research: Oceans*, *111*(C11).

Serreze, M. C., Crawford, A. D., Stroeve, J. C., Barrett, A. P., & Woodgate, R. A. (2016). Variability, trends, and predictability of seasonal sea ice retreat and advance in the Chukchi Sea. *Journal of Geophysical Research: Oceans*, *121*(10), 7308–7325.

Serreze, M. C., McLaren, A. S., & Barry, R. G. (1989). Seasonal variations of sea ice motion in the Transpolar Drift Stream. *Geophysical Research Letters*, *16*(8), 811–814.

Shibley, N. C., Timmermans, M.-L., Carpenter, J. R., & Toole, J. M. (2017). Spatial variability of the Arctic Ocean's double-diffusive staircase. *Journal of Geophysical Research: Oceans*, *122*(2), 980–994.

Sirevaag, A., & Fer, I. (2012). Vertical heat transfer in the Arctic Ocean: The role of double-diffusive mixing. *Journal of Geophysical Research: Oceans*, *117*(C7).

Smedsrud, L. H., Esau, I., Ingvaldsen, R. B., Eldevik, T., Haugan, P. M., Li, C., ... others (2013). The role of the barents sea in the Arctic climate system.

Reviews of Geophysics, *51*(3), 415–449.

Smith, K. S. (2007). The geography of linear baroclinic instability in Earth's oceans. *Journal of Marine Research*, *65*(5), 655–683.

Spall, M. A. (2013). On the circulation of Atlantic water in the Arctic Ocean. *Journal of Physical Oceanography*, *43*(11), 2352–2371.

Spall, M. A., Pickart, R. S., Fratantoni, P. S., & Plueddemann, A. J. (2008). Western Arctic shelfbreak eddies: Formation and transport. *Journal of Physical Oceanography*, *38*(8), 1644–1668.

Steele, M., & Boyd, T. (1998). Retreat of the cold halocline layer in the Arctic Ocean. *Journal of Geophysical Research: Oceans*, *103*(C5), 10419–10435.

Steele, M., Ermold, W., & Zhang, J. (2008). Arctic Ocean surface warming trends over the past 100 years. *Geophysical Research Letters*, *35*(2).

Steele, M., Morison, J., Ermold, W., Rigor, I., Ortmeyer, M., & Shimada, K. (2004). Circulation of summer Pacific halocline water in the Arctic Ocean. *Journal of Geophysical Research: Oceans*, *109*(C2).

Stein, R., Fahl, K., Gierz, P., Niessen, F., & Lohmann, G. (2017). Arctic Ocean sea ice cover during the penultimate glacial and the last interglacial. *Nature communications*, *8*(1), 373.

Stigebrandt, A. (1981). A model for the thickness and salinity of the upper layer in the Arctic Ocean and the relationship between the ice thickness and some external parameters. *Journal of Physical Oceanography*, *11*(10), 1407–1422.

Stommel, H. (1948). The westward intensification of wind-driven ocean currents. *Eos, Transactions American Geophysical Union*, *29*(2), 202–206.

Stommel, H. M. (1979). Determination of water mass properties of water pumped down from the Ekman layer to the geostrophic flow below. *Proc. Nat. Acad. Sci.*, *76*, 3051–3055.

Sverdrup, H. U., Johnson, M. W., Fleming, R. H., et al. (1942). *The oceans: Their physics, chemistry, and general biology* (Vol. 7). Prentice-Hall New York.

Timmermans, M.-L. (2015). The impact of stored solar heat on Arctic sea ice growth. *Geophysical Research Letters*(May). doi: 10.1002/2015GL064541.1.

Timmermans, M.-L., & Jayne, S. R. (2016). The Arctic Ocean spices up. *Journal of Physical Oceanography*, *46*(4), 1277–1284.

Timmermans, M.-L., Krishfield, R., Lee, C., & Toole, J. (2018). ALPS in the Arctic

Ocean. In D. Rudnick, D. Costa, K. Johnson, C. Lee, & M.-L. Timmermans (Eds.), *ALPS ii autonomous lagrangian platforms and sensors. a report of the ALPS ii workshop* (p. 37-39). La Jolla CA: 66 pp.

Timmermans, M.-L., & Ladd, C. (2019). [the Arctic] sea surface temperature [in “State of the Climate in 2018”]. *Bull. Amer. Meteor. Soc.*, *100*(9), S144-S146. doi: 10.1175/2019BAMSStateoftheClimate.1

Timmermans, M.-L., Marshall, J., Proshutinsky, A., & Scott, J. (2017). Seasonally derived components of the Canada Basin halocline. *Geophysical Research Letters*, *44*(10), 5008–5015. doi: 10.1002/2017GL073042

Timmermans, M.-L., Proshutinsky, A., Golubeva, E., Jackson, J. M., Krishfield, R., McCall, M., ... others (2014). Mechanisms of Pacific summer water variability in the Arctic’s central Canada Basin. *Journal of Geophysical Research: Oceans*, *119*(11), 7523–7548.

Timmermans, M.-L., Proshutinsky, A., Krishfield, R. A., Perovich, D. K., Richter-Menge, J. A., Stanton, T. P., & Toole, J. M. (2011). Surface freshening in the Arctic Ocean’s Eurasian Basin: An apparent consequence of recent change in the wind-driven circulation. *Journal of Geophysical Research: Oceans*, *116*(7). doi: 10.1029/2011JC006975

Timmermans, M.-L., Rainville, L., Thomas, L., & Proshutinsky, A. (2010). Moored observations of bottom-intensified motions in the deep Canada Basin, Arctic Ocean. *Journal of Marine Research*, *68*(3-4), 625–641.

Timmermans, M.-L., Toole, J., & Krishfield, R. (2018). Warming of the interior Arctic Ocean linked to sea ice losses at the basin margins. *Science advances*, *4*(8), eaat6773.

Timmermans, M.-L., Toole, J., Krishfield, R., & Winsor, P. (2008). Ice-tethered profiler observations of the double-diffusive staircase in the Canada Basin thermocline. *Journal of Geophysical Research: Oceans*, *113*(C1).

Timmermans, M.-L., Toole, J., Proshutinsky, A., Krishfield, R., & Plueddemann, A. (2008). Eddies in the Canada Basin, Arctic Ocean, Observed from Ice-Tethered Profilers. *Journal of Physical Oceanography*, *38*(1), 133–145. Retrieved from `http://journals.ametsoc.org/doi/abs/10.1175/2007JPO3782.1` doi: 10.1175/2007JPO3782.1

Toole, J., Krishfield, R., Timmermans, M.-L., & Proshutinsky, A. (2011). The

Ice-Tethered Profiler: Argo of the Arctic. *Oceanography*, *24*(3), 126–135. Retrieved from https://tos.org/oceanography/article/the-ice-tethered-profiler-argo-of-the-arctic doi: 10.5670/oceanog.2011.64

Toole, J. M., Schmitt, R. W., & Polzin, K. L. (1994). Estimates of diapycnal mixing in the abyssal ocean. *Science*, *264*(5162), 1120–1123.

Toole, J. M., Timmermans, M.-L., Perovich, D. K., Krishfield, R. A., Proshutinsky, A., & Richter-Menge, J. A. (2010). Influences of the ocean surface mixed layer and thermohaline stratification on Arctic sea ice in the central Canada Basin. *Journal of Geophysical Research: Oceans*, *115*(C10).

Tschudi, M., Fowler, C., Maslanik, J., Stewart, J., & Meier, W. (2016). Polar Pathfinder daily 25 km ease-grid sea ice motion vectors, version 3. *National Snow and Ice Data Center Distributed Active Archive Center, accessed February*.

Tulloch, R., Marshall, J., Hill, C., & Smith, K. S. (2011). Scales, growth rates, and spectral fluxes of baroclinic instability in the ocean. *Journal of Physical Oceanography*, *41*(6), 1057–1076.

Untersteiner, N. (1988). On the ice and heat balance in Fram Strait. *Journal of Geophysical Research: Oceans*, *93*(C1), 527–531.

Vihma, T., Screen, J., Tjernström, M., Newton, B., Zhang, X., Popova, V., … Prowse, T. (2016). The atmospheric role in the Arctic water cycle: A review on processes, past and future changes, and their impacts. *Journal of Geophysical Research: Biogeosciences*, *121*(3), 586–620.

Walsh, D., & Carmack, E. (2003). The nested structure of Arctic thermohaline intrusions. *Ocean Modelling*, *5*(3), 267–289.

Wettlaufer, J. (1991). Heat flux at the ice-ocean interface. *Journal of Geophysical Research: Oceans*, *96*(C4), 7215–7236.

Whitehead, J. (1998). Topographic control of oceanic flows in deep passages and straits. *Reviews of Geophysics*, *36*(3), 423–440.

Woodgate, R. A. (2018). Increases in the Pacific inflow to the Arctic from 1990 to 2015, and insights into seasonal trends and driving mechanisms from year-round bering Strait mooring data. *Progress in Oceanography*, *160*, 124–154.

Woodgate, R. A., & Aagaard, K. (2005). Revising the Bering Strait freshwater flux into the Arctic Ocean. *Geophysical Research Letters*, *32*(2).

Woodgate, R. A., Aagaard, K., Muench, R. D., Gunn, J., Björk, G., Rudels, B., ... Schauer, U. (2001). The Arctic Ocean boundary current along the Eurasian slope and the adjacent Lomonosov Ridge: Water mass properties, transports and transformations from moored instruments. *Deep Sea Research Part I: Oceanographic Research Papers*, *48*(8), 1757–1792.

Woodgate, R. A., Aagaard, K., Swift, J. H., Smethie Jr, W. M., & Falkner, K. K. (2007). Atlantic water circulation over the Mendeleev Ridge and Chukchi borderland from thermohaline intrusions and water mass properties. *Journal of Geophysical Research: Oceans*, *112*(C2).

Woodgate, R. A., Fahrbach, E., & Rohardt, G. (1999). Structure and transports of the East Greenland Current at 75 n from moored current meters. *Journal of Geophysical Research: Oceans*, *104*(C8), 18059–18072.

Woodgate, R. A., Stafford, K. M., & Prahl, F. G. (2015). A synthesis of year-round interdisciplinary mooring measurements in the bering strait (1990–2014) and the rusalca years (2004–2011). *Oceanography*, *28*(3), 46–67.

Woodgate, R. A., Weingartner, T., & Lindsay, R. (2010). The 2007 Bering Strait oceanic heat flux and anomalous Arctic sea-ice retreat. *Geophysical Research Letters*, *37*(1).

Woodgate, R. A., Weingartner, T. J., & Lindsay, R. (2012). Observed increases in bering Strait oceanic fluxes from the Pacific to the Arctic from 2001 to 2011 and their impacts on the Arctic Ocean water column. *Geophysical Research Letters*, *39*(24).

Worthington, L. (1953). Oceanographic results of project skijump i and skijump ii in the polar Sea, 1951–1952. *Eos, Transactions American Geophysical Union*, *34*(4), 543–551.

Wunsch, C. (2011). The decadal mean ocean circulation and Sverdrup balance. *Journal of Marine Research*, *69*(2-3), 417–434.

Yang, J. (2005). The Arctic and subarctic ocean flux of potential vorticity and the Arctic Ocean circulation. *Journal of Physical Oceanography*, *35*(12), 2387–2407.

Yang, J., Proshutinsky, A., & Lin, X. (2016). Dynamics of an idealized Beaufort Gyre: 1. the effect of a small beta and lack of western boundaries. *Journal of Geophysical Research: Oceans*, *121*(2), 1249–1261. doi:

10.1002/2015JC011296

Zhang, J., Rothrock, D. A., & Steele, M. (1998). Warming of the Arctic Ocean by a strengthened Atlantic inflow: Model results. *Geophysical Research Letters*, *25*(10), 1745–1748.

Zhang, J., & Steele, M. (2007). Effect of vertical mixing on the Atlantic water layer circulation in the Arctic Ocean. *Journal of Geophysical Research: Oceans*, *112*(C4).

Zhao, B., & Timmermans, M.-L. (2018). Topographic Rossby waves in the Arctic Ocean's Beaufort Gyre. *Journal of Geophysical Research: Oceans*, *123*(9), 6521–6530.

Zhao, M., & Timmermans, M.-L. (2015). Vertical scales and dynamics of eddies in the arctic ocean's canada basin. *Journal of Geophysical Research: Oceans*, *120*(12), 8195–8209.

Zhao, M., Timmermans, M.-L., Cole, S., Krishfield, R., Proshutinsky, A., & Toole, J. (2014). Characterizing the eddy field in the Arctic Ocean halocline. *Journal of Geophysical Research C: Oceans*, *119*(12), 8800–8817. doi: 10.1002/2014JC010488